

# Observation and modeling of eddies and dipoles in the Southern Indian Ocean

---

Yana Bebieva<sup>1</sup>  
Utrecht University

19.06.2013

## ***Abstract***

Analysis of the along track satellite data near the southern tip of Madagascar shows that the separation in this region occurs in the form of counter rotating pairs – dipoles. The integral of relative vorticity across the dipole's pathway is almost zero which supports the hypothesis that the western boundary current (WBC) is a source for the dipole formation, assuming the validity of the Stewart constraint for the WBC: the net relative vorticity across the WBC is zero.

For the numerical experiments three separation regions are chosen: the southern and northern tips of Madagascar as well as South Africa. It is shown that with the use of simplified linear and piecewise linear wind profiles, which are applied only for a 20-degree eastern sector of the domain, it is possible to generate at least three types of separation: shedding eddies from the southern tip of Madagascar, retroflexion of the Agulhas Current and a free jet from the northern tip of Madagascar.

Furthermore, slip and no-slip boundary conditions as they apply in Hallberg Isopycnal Model (HIM) are discussed here. It is shown that only under no-slip boundary conditions, isolated dipoles might be generated at the separation. Analysis of the integrals of relative vorticity across the western boundary layer and across the dipole's pathway in southern Madagascar illustrates that the source of dipoles at the separation is the WBC, which is in correspondence with observations.

---

<sup>1</sup> supervised and supported by: Prof. dr. W.P.M. de Ruijter and D. Le Bars

## Contents

1. General Introduction.....	3
1.1. Introduction .....	3
1.2. Physics of the boundary currents .....	5
2. Observing the along track satellite data .....	9
2.1. Introduction .....	9
2.2. Data description.....	10
2.3. Relative vorticity pattern along satellite track.....	11
2.4. Conclusion.....	12
3. Specificity of HIM model.....	13
3.1. Introduction .....	13
3.2. Representation of slip and no-slip BC.....	14
4. Numerical model set-up of the idealized experiments.....	16
5. Results of the simulation .....	22
5.1. Introduction .....	22
5.2. Simple rectangular domain experiment .....	22
5.3. Southern tips.....	25
5.3.1. Separation at the south of Madagascar.....	25
5.3.1.1. Explanation of the different behavior at separation for slip and no-slip conditions.....	28
5.3.1.2. Determination of meander period and wave period. Slip BC.....	29
5.3.1.3. Determination of eddy period and wave period. No-slip BC.....	33
5.3.1.4. Integral characteristic. Slip and no-slip.....	35
5.3.2. Agulhas retroflexion .....	38
5.4. Northern tip of Madagascar.....	45
5.4.1. Linear wind profile .....	45
5.4.2. Convergent wind profile .....	45
6. Summary and main conclusions .....	48
7. Acknowledgments.....	51
A1. Stream function evaluation .....	52
A2. Barotropic instability of the shear flow .....	52

# 1. General Introduction

## 1.1. Introduction

The current system in the Southern Indian Ocean is highly complex compared to the Sverdrup model of ocean circulation. From the observations, the average wind stress curl over the Southern Indian Ocean is negative to the north of approximately 18° S and positive to the south of this latitude (Figure 2b, Backeberg et al., 2012). So, the wind pattern in this area may be roughly approximated by a cyclone in the north and an anticyclone in the south (Figure 1). The southern side of the cyclonic flow and the northern part of the anticyclonic flow create easterly and associated South Equatorial Current (SEC) at around 18° S. Such wind stress causes a circulation of two gyres in the same sense as the wind stress curl. That is, in order to compensate the input of positive (negative) vorticity from the wind stress, the water masses move northward (southward) in the interior and acquire negative (positive) vorticity through the  $\beta$ -effect. This northward (southward) motion is compensated by swift narrow return currents to the north and to the south of 18° S respectively.

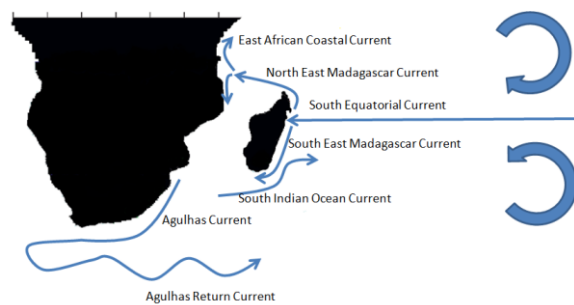


Figure 1. Schematic of main surface currents in the Southern Indian Ocean. Thin lines – currents; thick arrows – wind;

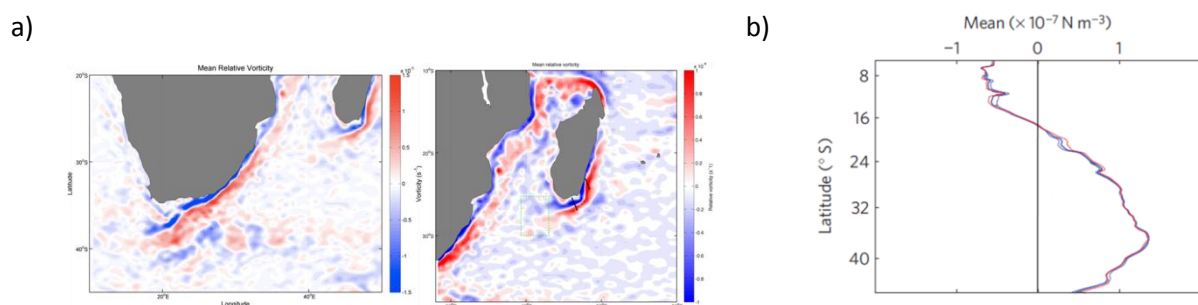


Figure 2. a) Averaged over 20 years relative vorticity patterns (within the color range  $\pm 1.5 \cdot 10^{-5} \text{ s}^{-1}$  for Madagascar and  $\pm 10^{-5} \text{ s}^{-1}$  for the South Africa) in the southwest of Indian Ocean. Adopted from Ridderinkhof et al. 2013. b) Zonal mean wind-stress curl for 1993–1999 (blue) and 2003–2009 (red) for 15–120 E. Adopted from Backeberg et al., 2012.

The North East Madagascar Current (NEMC) leaves the northern tip of Madagascar and starts meandering westward after separation and subsequently joining the East African Coastal Current (LaCasce et al. 2007; de Ruijter et al. 2004). The southward boundary current is called the South East Madagascar Current (SEMC). According to several authors (Quartly et al., 2006; Gründlingh, 1995 and others) it follows the eastern coast of Madagascar until the very south of the island, detaches

from it and then provides source water to the Agulhas current. However Lutjeharms (1976), after finding water masses of central Indian Ocean origin in the Mozambique channel, states that some part of SEMC should do a substantial trip (a few hundred kilometers) to the north after wrapping around the southern tip and only then it joins the Agulhas current system. Another supposition is that there is a retroflection to the south of Madagascar with the possibility of eddy shedding from this loop (Lutjeharms et al., 1981 and others). Recent work based on remote-sensing observations indicates that a regular series of symmetric vortex pairs propagate from the tip of South Madagascar, mainly in the southwest direction (Figure 3, Ridderinkhof et al. 2013). Subsequently, many of these eddies join the Agulhas Current. Also, during a hydrographic cruise in March 2001, a dipole-like vortex structure was measured southwest of Madagascar (de Ruijter et al. 2004).

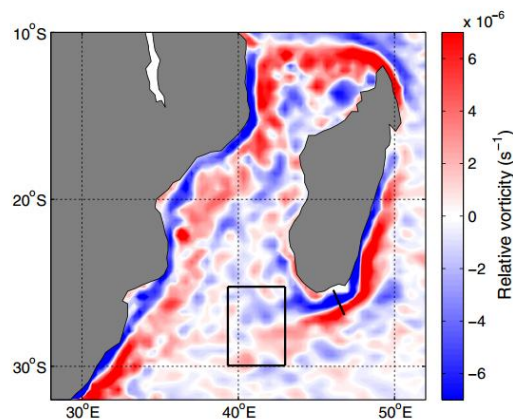


Figure 3. Mean relative vorticity around Madagascar. Taken from Ridderinkhof et al. 2013.

The flow regime to the south of Madagascar has been often compared to the Agulhas current. However this boundary current, once reaching the southern point, does not continue to the west but turns back and moves eastward while shedding eddies. The Agulhas Rings move into the South Atlantic.

The southwest Indian Ocean experiences substantial variability in the form of meanders and eddies. The currents in this region were modeled both analytically and numerically by many authors (LaCasce et al. 2007, J. C., etc.). In numerical models, the western boundary current (WBC) separation mechanism is very sensitive to various parameters and there is no unique method that seems to fit all western boundary separations (Chassignet and Marshall, 2008). The boundary conditions (BC) (slip or no-slip) influence the separation latitude (Chassignet and Marshall, 2008) as well as the behavior of the separation (Dengg, 1992). The separation occurs earlier and more abruptly with no-slip than with slip conditions (Kiss, 2002). Although at the boundary there are no

velocity discontinuities and therefore the real ocean does not slip at continental boundary, some models with slip BC produce more realistic simulations (Stewart, 1989).

In this study we focus again on the control of the BC on boundary current separation in ocean models and the physics that play a leading role in the separation process of the real NEMC, SEMC and Agulhas current. We use the observed flow fields from 20 years of satellite altimetry and the analysis of Ridderinkhof et al. (2013).

One of the questions of this study is to what degree the far field produces different separation characteristics: dipole formation, a free jet or retroflexion. The second one is what kind of lateral boundary conditions, either no-slip or free slip, is more suitable for simulating reality in numerical modeling.

To achieve this goal we started from the most basic structure - barotropic homogeneous ocean with flat frictionless bottom under constant wind curl forcing. Several types of wind are applied in order to simulate different cases of separation, representative for the NEMC, SEMC and Agulhas current. We use very simplified wind profiles – linear and piecewise linear applied only to the eastern part of the basin. Even such simplified cases lead to unexpected results which have to be taken into consideration while using the more complex models.

In Section 1.2 an explanation of the dynamics of the boundary layer formation is given. Section 2 focuses on the data retrieval from along track satellite altimetry around southwest Madagascar in order to define a general structure of the flow there. In this section the following questions are answered; What is a relative vorticity pattern across the dipole pathway and does it fit the theory (Stewart constraint, 1989)? In Section 3 the model specificity is presented such as implementation of BC, integration scheme. Section 4 and Section 5 deal with numerical experiments. Hereby the following questions underlie; May far field be responsible for the eddy generation at the tips? What are the main differences in the slip and no-slip experiments? What is the eddy shedding period and how does it correspond to basin modes? Finally, in Section 6 a summary and the main conclusions are presented, here the leading questions of this report are answered.

## 1.2. Physics of the boundary currents

In order to solve the non-linear second order momentum equations, two boundary conditions have to be specified. The first one is the condition of no flux, the second one is either free slip

( $\frac{\partial \vec{u}}{\partial \vec{n}} = \zeta = 0$ ) or no-slip ( $\vec{u} = 0$ ); all symbols are defined in Table 1. The problem of slip and no-slip

boundary conditions as they apply to ocean models is a controversial issue nowadays. To understand

the impact of each lateral boundary condition on the physics of the WBL, consider governing processes that take place there.

The description of the dynamics of the Sverdrup flow in the ocean gyre is given in various literature, such as the books of Pedlosky (1996) and Dijkstra (2008) and its derivation will not be presented. Here, we start directly from the vorticity equation for barotropic homogeneous ocean with a flat frictionless bottom.

In the HIM model the governing equations are written in isopycnal coordinates, however to get a feeling about the process the discussion below will be based on the equations in Cartesian coordinates. (Note: bottom friction is not included; more about model parameters will be discussed in Section 3).

From Pedlosky (1996) the vorticity equation is

$$\frac{\partial \zeta}{\partial t} + \vec{u} \cdot \vec{\nabla} \zeta + \beta_0 v = \vec{k} \cdot \frac{\nabla \times \tau}{\rho_0 H_0} - A_H \nabla^2 \zeta \quad (1.1)$$

*ADV    BETA    WIND    VIS*

Where *ADV* denotes the nonlinear advection term, *BETA* the planetary vorticity term, *WIND* the wind stress vorticity, *VIS* the viscosity term and all symbols are defined in Table 1.

**Table 1. Symbol definitions**

$\vec{u} = (u, v)$	vertically integrated horizontal velocity
$\zeta = \frac{\partial v}{\partial x} - \frac{\partial u}{\partial y}$	relative vorticity
$t$	time
$f = f_0 + \beta_0 y$	planetary vorticity
$\vec{k}$	unit vertical vector
$\tau$	wind stress vector
$\rho_0$	reference density, $\rho_0 = const$
$H_0 = 1000m$	constant depth
$A_H$	coefficient of turbulent horizontal diffusion
$\nabla = \left( \frac{\partial}{\partial x}, \frac{\partial}{\partial y} \right)$	horizontal gradient operator
$\vec{n}$	local coordinate normal to the boundary

Based on the potential vorticity (PV) analysis as in the work by Nakano et al (2008) for the Kuroshio Current System with the usage of no-slip lateral BC, the analysis for the SEMC-like currents in context of one-gyre system will be given below. Here the PV is defined as  $PV = \frac{f + \zeta}{H_0}$ . The vorticity

balance in the boundary current for the linear Munk model is  $VIS = BETA$ . Therefore, in the linear model the flux of the vorticity into the western boundary layer (WBL) balances the vorticity input by the wind. However advection becomes important when nonlinearity is introduced by the swift narrow current. In the inertial sublayer the viscosity term is negligible and therefore  $BETA = -ADV$ . So the fluid tends to preserve its PV in the sublayer. That means that the anomalously high values of PV appear within this sublayer. Thus, in the outer WBL, PV is increased by the anticyclonic relative vorticity, therefore, the flow is “dragged” southward in order to acquire required PV to join interior. This process may delay the fluid’s PV recovery while moving southward, this phenomenon is usually called the “crisis” due to insufficient recovery of PV (Kiss, 2002). In the viscous sublayer the balance is as  $VIS \approx BETA + ADV$ , so while fluid moves southward it obtains more negative vorticity than is needed to join the interior ( $VIS > BETA$ ), therefore, there will be anomalously low PV in the viscous sublayer; it becomes as an opposite “crisis”.

According to these arguments, at the separation position, the boundary flow contains anomalously low PV in the inshore zone and anomalously high PV in the offshore sublayer. If this reasoning is translated into relative vorticity distribution then, on the shore side the negative relative vorticity will be accumulated and on the sea side positive relative vorticity, as shown in Figure 4.

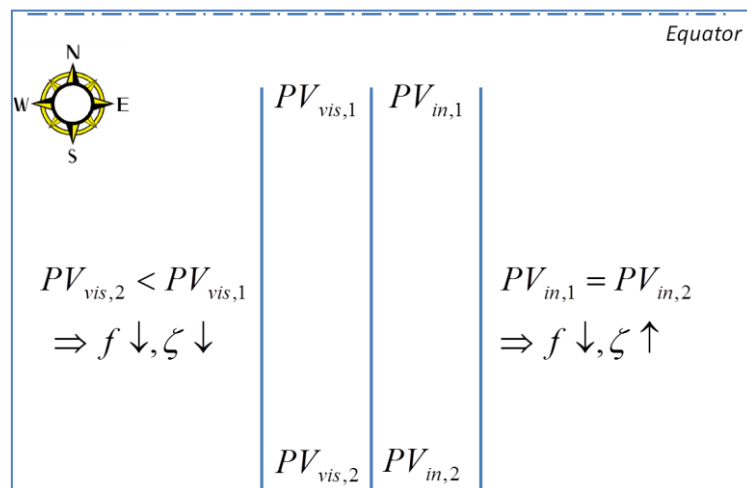


Figure 4. Diagram of PV distribution in the WBL (South Hemisphere).  $PV_{vis}$  – potential vorticity within viscous sublayer,  $PV_{in}$  - potential vorticity within inertial sublayer. Here both sublayers are of equal width only for the simplicity of drawing.

In such a configuration, before the flow joins the interior it needs to dissipate extra PV in the viscous sublayer. It causes the origin of the cyclones at separation.

It is worth mentioning that only some part of the current goes through the viscous sublayer, the remaining current flows through the outer inertial sublayer. As described in Pedlosky (1996), the streamlines that enters only the inertial flank, leave the western coast not as a concentrated current, but individually when each streamline has gained enough relative vorticity to connect to the interior. The position where the flow exits the WBL highly depends on the length scale of the subinertial layer. It is nicely shown in the work by Kiss, 2002 that at a large inertial boundary layer the mismatch in PV between the WBL and interior becomes so large that fluid must change trajectory significantly in order to find suitable latitude to get out of the WBL.

According to Stewart (1989), if no-slip BC is applied to the western boundary – “boundary currents neither contain nor transport relative vorticity” when the whole width of the current is considered. It takes place because the total relative vorticity ( $Z$ ) is an integral of relative vorticity ( $\zeta$ ) from the lateral boundary ( $x=b$ ) where meridional velocity ( $V$ ) is zero by definition of the no-slip conditions, towards the position where boundary current ends ( $x=w$ ), i.e. where zonal velocity is again zero.

$$Z = \int_b^w \zeta dx$$

The situation is similar for vorticity transport ( $Q$ )

$$Q = \int_b^w \zeta V dx$$

This result comes from the observed fact that there are two zones within the WBL: one of negative relative vorticity and the other one of positive relative vorticity. Based on that, one might hypothesize that such a construction of the boundary current leads to the generation of symmetric dipole structure at separation.

Totally different behavior is found for the cases where slip BC is applied. There will be no anomalously low PV on the shore side; the entire boundary current is anticyclonic contrary to the recent observations.

## 2. Observing the along track satellite data

### 2.1. Introduction

Assuming geostrophic balance (explained further in this section), prominent signatures of eddies in sea surface height (SSH), have allowed the usage of satellite altimetry in observing global ocean variability. In this study, to observe a spatial variability of the ocean near the African and Madagascar tips along track data is used. In this case satellite radar altimeter provides a snapshot of an SSH profile along its ground tracks, revealing the ocean structure that is not available from in situ observations (Fu et al., 2010).

Assume geostrophic and hydrostatic balance (Pedlosky, 1987)

$$\rho_0 f \vec{k} \times \vec{u} = -\nabla p \quad (1.2)$$

$$\frac{\partial p}{\partial z} = -\rho_0 \vec{g} \quad (1.3)$$

Where  $z$  – vertical coordinate,  $\vec{g}$  - gravitational acceleration,  $p$  - pressure field and others symbols are determined in Table 1. Combination of equations (1.2) and (1.3) gives

$$\vec{k} \times \vec{u} = \frac{g}{f} \nabla \eta \quad (1.4)$$

where  $\eta$  is the absolute dynamic topography, the elevation of the free surface of the ocean, relative to the geoid. Since geoid is the best representation of the Earth's sea surface in the absence of any motion, then from absolute dynamic topography the geostrophic flow might be derived and relative vorticity pattern from the geostrophic flow as

$$\zeta = \frac{\partial v}{\partial x} - \frac{\partial u}{\partial y} \quad (1.5)$$

Here, the along track data is needed for analysis of relative vorticity structure of the flow after the separation, mainly the integral characteristics across the separated jet. Three satellite tracks are available near south Madagascar (Figure 5). The most interesting track is # 120, because it is normal to the flow and the velocity tangential to the track might be neglected.

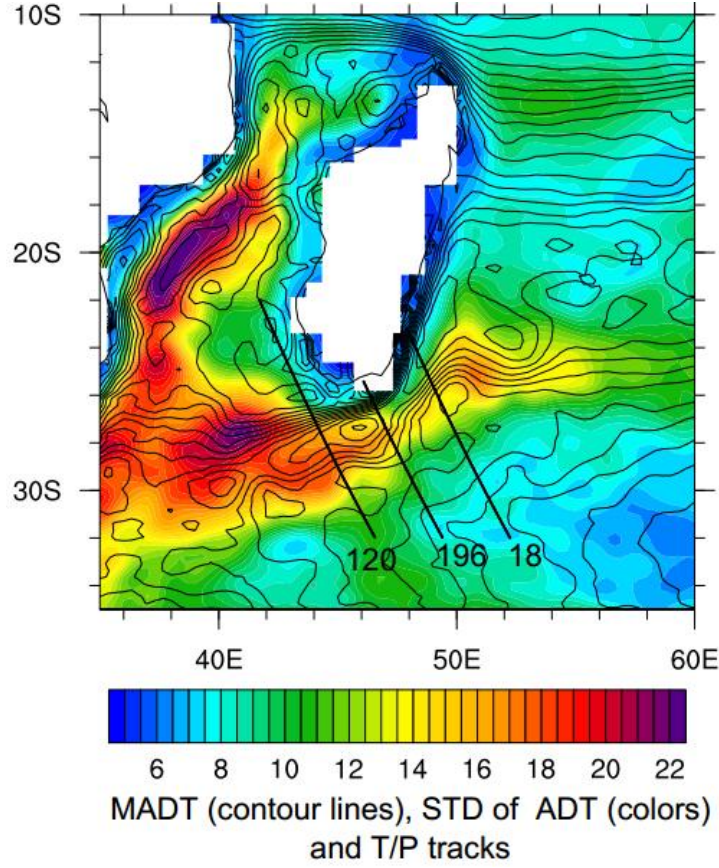


Figure 5. Satellite tracks used in the research.

In this case, along track calculations formulas (1.4), (1.5) need to be modified, since there is only one horizontal coordinate that aligns with the track. Then the velocity normal to the track is found by

$$v_n = \frac{g}{f} \frac{\partial \eta}{\partial l} \quad (1.6)$$

where  $\partial l$  - spatial step along track. And the relative vorticity is

$$\zeta = \frac{\partial v_n}{\partial l} \quad (1.7)$$

## 2.2. Data description

The altimeter products were produced by Ssalto/Duacs and distributed by the Archiving, Validation and Interpretation of Satellite Oceanographic data base (AVISO), with support from the French Centre National d'Etudes Spatiales (<http://www.aviso.oceanobs.com/duacs/>). Along track satellite data provides the absolute dynamic topography ( $\eta$ ) and the sea surface anomaly (SSA).

The along-track satellite observations that are used have a repeat orbit of 9.9156 days. The analyzed satellite tracks are observed by three different satellites following the same orbit, the

Topex/Poseidon satellite from September 1992 until September 2002, the Jason-1 satellite from September 2002 until June 2008 and the Jason-2 satellite from June 2008 until November 2010.

### 2.3. Relative vorticity pattern along satellite track

As mentioned above, track # 120 is the handiest one since it crosses perpendicularly the jet that originates from the separation area. It is expected that the integral characteristics across this jet are the same as upstream in the SEMC. If the boundary current has a structure like as described in Section 1.2 then the WBL does not contain net relative vorticity, therefore there should be no relative vorticity across the southwestward jet either.

In order to verify the above mentioned fact, several regions along track # 120 were chosen (Table 2).

**Table 2. The description of the regions chosen for relative vorticity analysis**

Distance	The range includes	$\frac{\int_{range} \zeta dl}{\int_{range} dl}, [s^{-1}]$
whole distance (1197 km)	Main jet, retroflexion, northern and southern fluctuations	$-0.48 \cdot 10^{-7}$
between 26° S and 30° S (486 km)	main jet and retroflexion	$-4.54 \cdot 10^{-7}$
between 26° S and 28° S (243 km)	main jet	$-1.06 \cdot 10^{-7}$

Velocity normal to the track is calculated using (1.6) and subsequently the relative vorticity field is reconstructed with (1.7) for each snapshot. Then, the data is integrated over the length of each zone with trapezoidal numerical integration scheme and finally it is averaged in time. The trapezoidal rule works by approximating the region under the graph of the function as a trapezoid and calculating its area. In the given case, each trapezoid is constructed on the neighboring points of the data, the area of each trapezoid is calculated and subsequently all areas are summed up. In order to compare results, the obtained integrals were normalized on the length of each sector, i.e. integral of relative vorticity that is averaged in time is divided by the length of the zone (Table 2, right column).

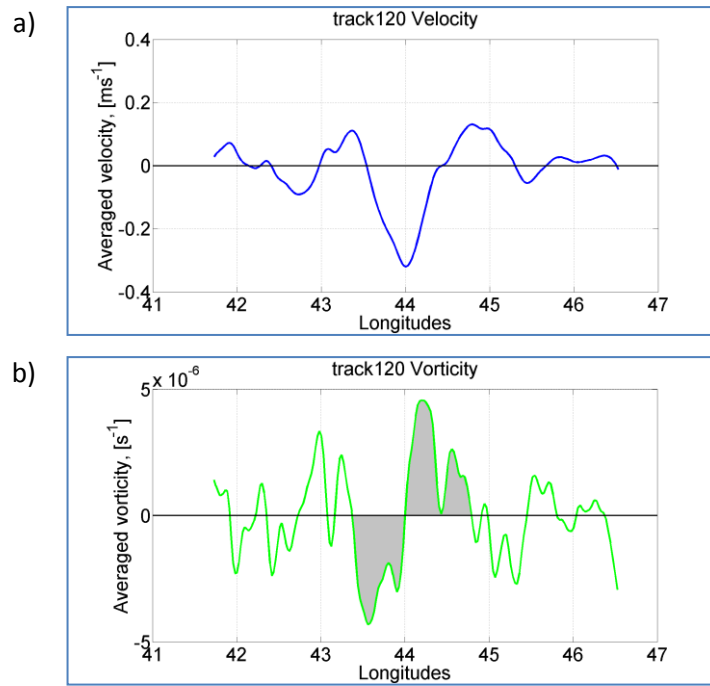


**Figure 6. Averaged over 20 years velocity and relative vorticity distribution along track # 120. The values are calculated from absolute dynamic topography of altimetry data.**

The smallest absolute value of these three integrals belongs to the whole distance of the track. However, this zone covers the area beyond the main jet and its retroflexion where not much motion was observed, as a consequence there is almost zero relative vorticity input to the integral. That levels off the value of the normalized integral. The integral along the zone that covers the main jet and retroflexion shows a bigger absolute value than for the main jet region. It is probably because positive relative vorticity, which theoretically comes from the inertial sublayer, is compensated by negative relative vorticity at the same streamlines which originated after separation.

Figure 5 shows that the magnitude of relative vorticity fluctuation is of the order  $10^{-6} \text{ s}^{-1}$ , that is around ten times more than the normalized integral values. Thus, based on these results it might be considered that the integral of relative vorticity along track # 120 across the main jet is almost zero, yet shifted to the negative side a little bit.

Figure 5a) shows the symmetry in the velocity and vorticity fields. Since it is known that the area where track # 120 lies is highly dynamic (Ridderinkhof et al. 2013), the symmetry of these fields indicate that counter-rotating eddies (dipoles) with similar length scale frequently crosses this line.

## 2.4. Conclusion

It is shown that at the southern tip of Madagascar the separation occurs in the form of counter rotating pairs – dipoles (Figure 6). The normalized value of integrated relative vorticity across this

part of track # 120, normal to the dipole's pathway is almost zero. When the Stewart constraint (1989) is valid for the WBL, then the integral of relative vorticity is zero within the WBL, and the data shows that the flow retains this property while propagating southwestward. It is impossible to check the applicability of the Stewart constraint for the WBL from satellite data because the SEMC lies too close to the shore where the geoid is not well known. However, a structure of the WBL with positive onshore and negative offshore relative vorticity and a similar structure of velocity and vorticity patterns from the data support the WBL as a source for the dipole formation.

During a hydrographic cruise in March 2001, the dipole with similar characteristics to those shown above was found southwest of Madagascar (de Ruijter et al., 2004). However, there is some difference in the magnitude of the relative vorticity. De Ruijter et al. (2004) state that relative vorticity in the center of cyclonic and anticyclonic eddies is around  $2 \cdot 10^{-5} \text{ s}^{-1}$  and outside the dipole the vorticity variation is of the order  $0.5 \cdot 10^{-5} \text{ s}^{-1}$ . Yet in the time averaged case (Figure 6b), the relative vorticity in the center of eddies reaches only  $0.5 \cdot 10^{-5} \text{ s}^{-1}$  because eddies do not all have the same path and they are not there all the time.

### 3. Specificity of HIM model

#### 3.1. Introduction

For the purpose of modeling, the HIM model was used. It is a C-Grid isopycnal coordinate primitive equation ocean model. Hereby only important (in the frame of this report) characteristics of the model will be discussed. More detailed specification of the model can be found in the model description by R. Hallberg (1997).

The numerical method used in the model is the split-explicit time stepping scheme (Hallberg, 1997); with this scheme HIM exactly conserves the mass, potential vorticity and energy of each isopycnal layer, unless the diapycnal mixing is explicitly parameterized, which is done in this work. The model allows for turbulent entrainment and the full nonlinear equation of state is used. Wind stress is imposed as a stress BC at the upper surface. (Hallberg 2005).

For the viscosity term there are three possibilities: Laplacian, Biharmonic (in combination with Laplacian) and Smagorinsky. In the present work only Laplacian horizontal viscosity is used, which refers back to the work of Munk (1950), who assumed that eddy viscosity is isotropic 'neglecting variations that might be related to differences between zonal and meridional motions of large horizontal eddies on a rotating earth'. Thus, horizontal friction in the momentum equation has the Laplacian form  $\nabla \cdot A_M \nabla \vec{u}$ , where  $A_M$  - is an isotropic viscosity.

Since the purpose of this work is to apply various BC – slip, no-slip, the determination of BC will be discussed in detail further.

### 3.2.Representation of slip and no-slip BC

At the lateral boundaries, either free slip or no-slip BC are applied in the model.

The full formula for calculation of relative vorticity  $\zeta_{i,j}$  at position  $(i, j)$  is

$$\zeta_{i,j} = \frac{v_{i+1/2,j} - v_{i-1/2,j}}{a \cos \theta_j \Delta \phi} - \frac{\cos \theta_{j+1/2} u_{i,j+1/2} - \cos \theta_{j-1/2} u_{i,j-1/2}}{a \cos \theta_j \Delta \theta} \quad (1.8)$$

where  $v$  is a meridional velocity on Arakawa C-grid,  $u$  - a zonal velocity on Arakawa C-grid,  $a$  - radius of the Earth,  $\theta_j$  - latitude,  $\Delta \phi$  - zonal resolution,  $\Delta \theta$  - meridional resolution.

At the western boundary with a no-slip BC the relative vorticity becomes

$$\zeta_{i,j} = (2v_{i+1/2,j}) / (a \cos \theta_j \Delta \phi) \quad (1.9)$$

In this case  $v_{i+1/2,j}$  is the first meridional velocity point at water. In this formula there is no zonal velocity because it is set to zero at boundaries, whereas there is no such condition for the meridional velocity due to specificity of Arakawa C-grid, the tangential velocity is not specified. To impose a zero tangential velocity at the coast, a mirror velocity point ('ghost' point) is defined inland of the boundary, and its value is set to the opposite of the tangential velocity component seaward of the coast, thus delivering a no-slip condition on the coast. Note that this mirror velocity point is not visible in the output files; it is simply replaced by zeros for the output.

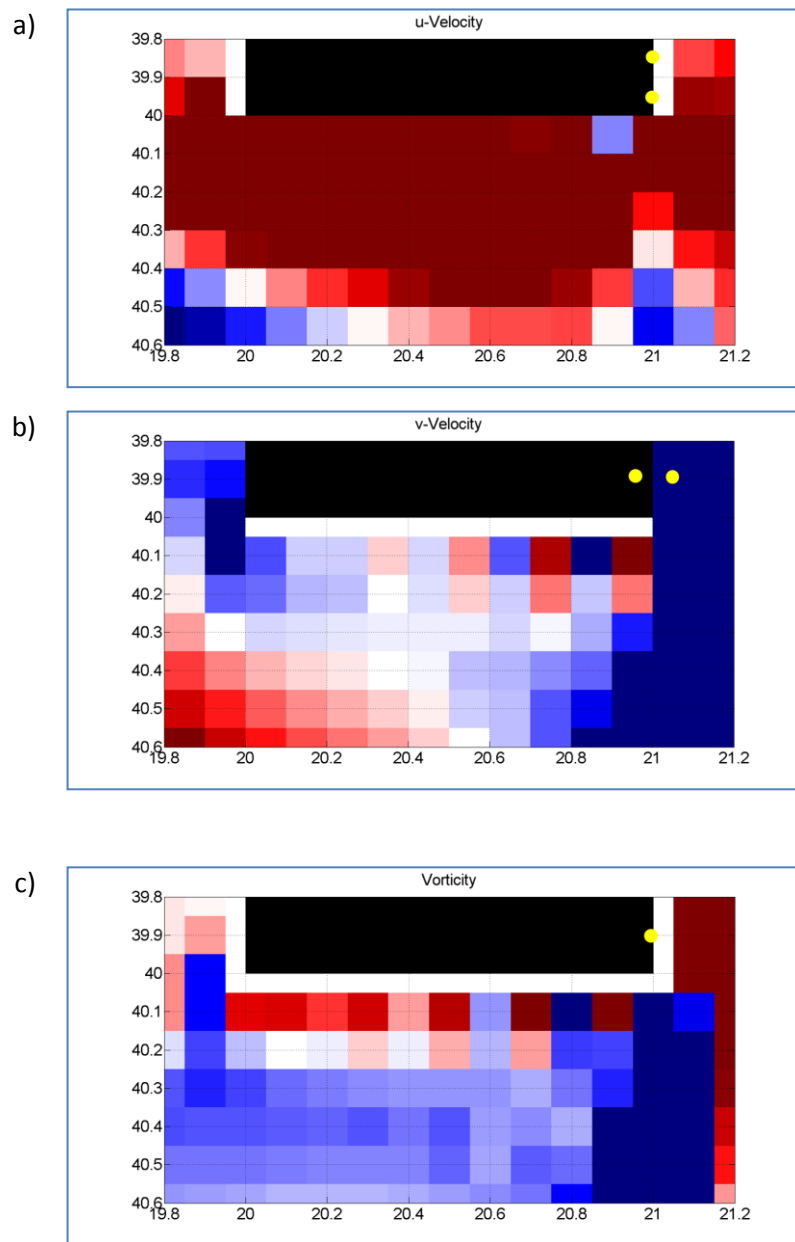


**Figure 7. Example of Arakawa C-grid for three variables: a) zonal velocity, b) meridional velocity and c) relative vorticity. Yellow points on (a) and (b) panels indicate points that are needed for calculation of relative vorticity at yellow position on (c) panel.**

In Figure 7, an example of variables (zonal velocity, meridional velocity and relative vorticity) on the Arakawa C-grid is shown, and it is visible that grid cells for each variable are shifted relative to each other. In order to compute the value for relative vorticity (yellow point on Figure 7c), two points of zonal velocity (u-velocity, Figure 7a) and two points of meridional velocity (v-velocity, Figure 7b) are used. In this figure, it is also seen that relative vorticity along all boundaries is zero, which does not correspond to the description of the model (Hallberg, 1997). In order to fill these gaps for the

western boundary, manually calculated values for relative vorticity with the formula (1.10) was used for no-slip cases.

For slip case  $\zeta_{i,j} = 0$  at boundaries, therefore it is possible to use pure data from the output files of the HIM model.

#### 4. Numerical model set-up of the idealized experiments

The domain considered is a closed rectangular basin with a simplified continent in the northwest in some sets of experiments and in the southwest in others. In total, 70 experiments were carried out during this research. They differ by BC (slip, no-slip), resolution, the Laplacian horizontal viscosity (just 'viscosity' later on), wind configuration, and geometry. Note that only one type of BC may be applied to the domain for one simulation, in this way if no-slip is chosen then it is set to the land boundary and to the domain boundary as well; similar for the slip BC. The flow is driven with a constant wind forcing in time, the wind stress is  $\tau = 0.3Pa$  in all experiments. Overall, five configurations of the wind force were examined; all of them have either a linear or piecewise linear profile. So the separation would not be influenced by the local forcing, the far field wind forcing is applied only on the eastern 20 degrees of the domain, which is quite far (20 degrees) from the land parts (land configurations are described further). The constant depth is 1000m. The thickness of the bottom boundary layer is set to zero, i.e. bottom friction is not included.

The barotropic and baroclinic time steps are  $30s$  and  $240s$  for most of the experiments unless the resolution is too small ( $<1^\circ$ ) or the viscosity has small values ( $A_M < 100m^2s^{-1}$ ), in this case the time steps reduce to  $15s$  and  $150s$ .

The results are saved in the 10-day averages sets for all variables. The total simulation time is 1800 days (around 5 years). The spin up time is approximately one year for all experiments. The model was integrated to a statistically steady state, as revealed from the integral kinetic energy. Mean fields were calculated over 1390 days in order to average out the transients. However, the time series' were produced to see the evolution of some specific features.

There are two main configurations of experiments. The first one was created to model the south Madagascar separation and Agulhas current, the second one to simulate the north Madagascar separation.

For the "south" experiments, three wind structures were considered on the basin which extends from  $0^\circ$  to  $60^\circ E$ ,  $20^\circ$  to  $60^\circ S$ . The land is represented as a rectangular area between  $20^\circ$  and  $21^\circ E$ ,  $20^\circ$

and 40°S. The first set of experiments has a linear wind profile with a constant anticyclonic wind curl (Figure 8a). This wind is expected to produce a clear western boundary current along the land which separates at the southern tip afterwards. According to the theory, the flow may return to the interior only as the western boundary current. Therefore, after separation at the southern tip, flow has to move westward conserving its PV, and once it reaches the domain western boundary it flows along it and joins the interior via south (Figure 18). With this experiment the separation mechanism under slip and no-slip conditions is examined. Also several viscosities are tested.

For the second configuration the wind curl is constant and negative for the northern part of the basin (this part changes while performing sensitive experiments) and there is no wind curl for the rest (Figure 8b). This wind forcing allows a return current at the latitudes when the wind curl goes to zero. Therefore, there might be interaction between the return current and the separated WBC, which may end up in the retroflexion which takes place in the Agulhas current system.

The third set of experiments is constructed in a way that a wind curl changes from negative to positive at the certain latitude of the domain – divergent structure (Figure 8c); this latitude is varied for sensitivity experiments too. Note that while varying the zero wind curl position, the magnitude of the curl of the southern and northern part remains the same, i.e. this variation works as a parallel shifting. This construction may produce retroflexion at the zero wind curl position as well as in the second wind type.

For the modeling of the northern separation two wind configurations were studied on a domain that lies from 0° to 60°E and from 10°N to 30°S. The land is again a one-degree zone which extends from 20° to 21°E, 10° to 30°S. The first wind structure is linear with constant negative curl over the domain (Figure 9a). The purpose of this experiment is an attempt to observe a separation of WBL in the form of dipoles at the northern tip.

The second structure is a piecewise linear wind – convergent wind – with negative curl over the southern part and positive curl over the northern part of the basin (Figure 9b). This wind type produces the jet at the latitude where the wind curl changes sign. The jet interacts with the separated WBL and it is likely that it suppresses the eddy generation in this area.

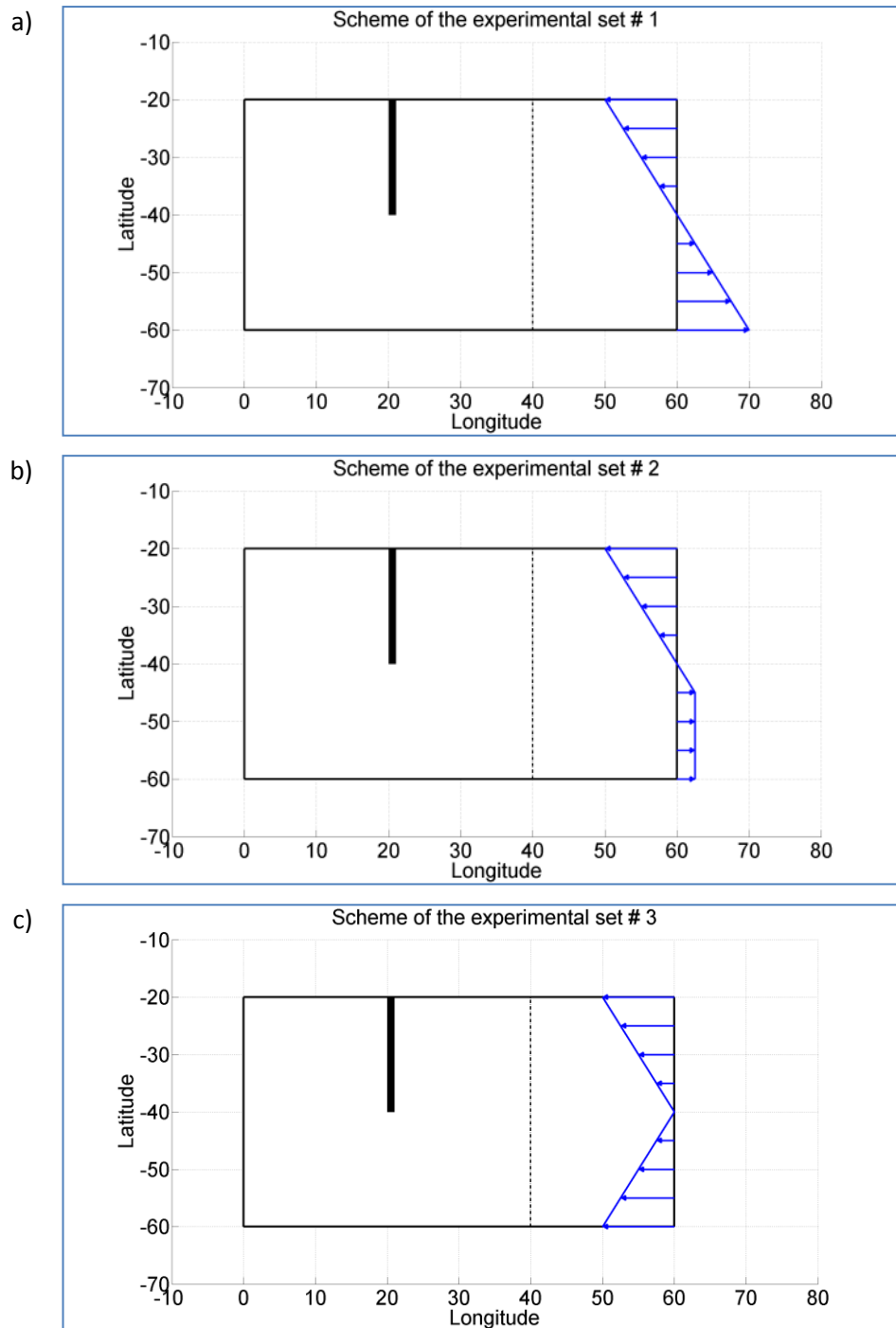


Figure 8. Experimental schemes for the simulation of the southern Madagascar separation. Positive values of longitudes stand for the east longitudes, negative for west longitudes; negative values of latitude mean southern latitude. Each panel shows a top view of the domain. Black shaded area represents land between 20° and 21°E, 20° and 40°S. The wind is schematically drawn by blue arrows on the eastern boundary. Dashed line indicates longitude until which wind forcing is applied from the east boundary, i.e. in between 40° and 60°E; the forcing is zonally uniform within this 20 degrees.

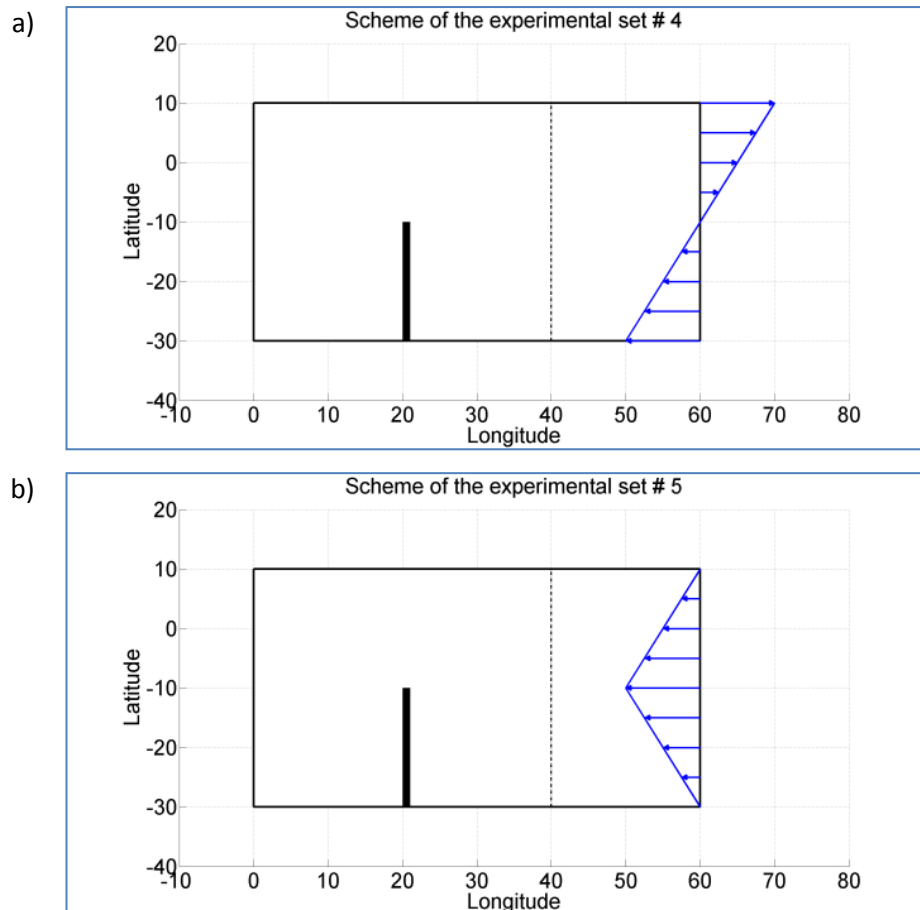


Figure 9. Same as Figure 8 but these experimental schemes for the simulation of the northern Madagascar separation. Black shaded area represents land between 20° and 21°E, 10° and 30°S.

The summary of the experiments are in the Table 3.

Moreover apart from the study of different wind structures and a various geometry of the domain, a simple rectangular domain model forced by a constant wind curl over 20 eastern degrees of the domain is considered (Figure 10). This scheme is constructed in a way that there is the western boundary of the domain instead of the land at 21°E. This simple structure is set in order to examine the WBL in the absence of the land and reveal features that are peculiar for such basins. In this experiment: no-slip condition is applied to the boundaries, the viscosity is  $\nu$  and other parameters are as described above.

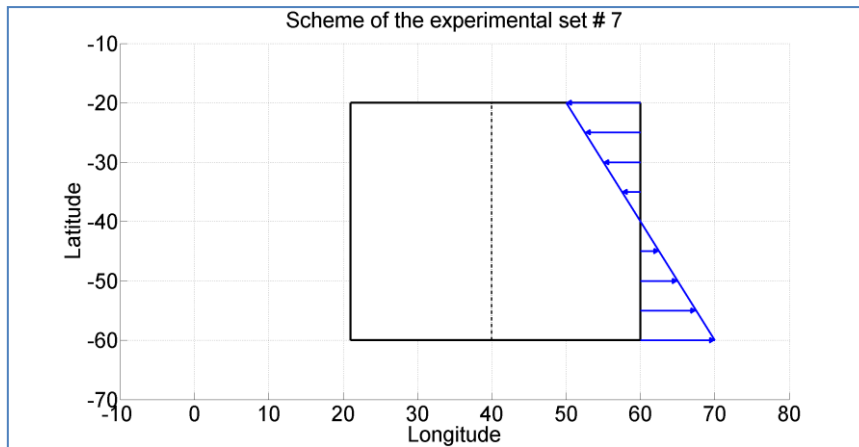


Figure 10. Same as Figure 8 but this experimental scheme for the rectangular domain model experiment with linear wind profile (constant anticyclonic curl).

Table 3. Summary of the experiments.

Name of experiment set	Short description	Laplacian horizontal viscosity used, [ $\text{m}^2 \text{s}^{-1}$ ]	BC used	Diagram
Exp. set # 1	<ul style="list-style-type: none"> <li>• Usage the same wind structure;</li> <li>• Various resolution 0.05° and 0.1°</li> <li>• Change of viscosity;</li> <li>• Application of two types of BC: slip and no-slip.</li> </ul>	500 300 250 200 150 100	slip no-slip	
Exp. set # 2	<ul style="list-style-type: none"> <li>• Change of the wind structure by shifting the zero wind curl position; latitude range from 40°S to 46°S.</li> <li>• Change of viscosity;</li> <li>• Application of no-slip BC only</li> </ul>	500 300 250 200 150 100	no-slip	
Exp. set # 3	<ul style="list-style-type: none"> <li>• Usage only one viscosity;</li> <li>• Change of the wind structure by shifting the zero wind curl position; latitude range from 38°S to 46°S. Wind curl remains the same;</li> <li>• Application of no-slip BC only</li> </ul>	100	no-slip	
Exp. set # 4	<ul style="list-style-type: none"> <li>• Usage only one viscosity;</li> <li>• Application of no-slip BC only</li> </ul>	100	no-slip	
Exp. set # 5	<ul style="list-style-type: none"> <li>• Usage only one viscosity;</li> <li>• Change of the wind structure by shifting the zero wind curl position; latitude range from 4°S to 16°S. Wind curl remains the same;</li> <li>• Application of no-slip BC only</li> </ul>	100	no-slip	

## 5. Results of the simulation

### 5.1. Introduction

The output of the HIM model is delivered by NetCDF files, containing a wide variety of instantaneous and time averaged diagnostic fields. Since we are mostly interested in the statistically steady state of phenomena, the time averaged values will be mainly used in the further analysis. Note that saving of files took place every 10 model days; therefore we will deal with 10-day averaged sets of data. Relative vorticity, velocity and sea surface height fields are substantially used in the report.

In this section the results of numerical simulations with several methods of their analysis will be presented.

### 5.2. Simple rectangular domain experiment

For the simple rectangular domain experiment, anticyclonic wind stress over the eastern part of the domain (from 40°E to 60°E) drives a uniform northward Sverdrup flow, which is returned as the narrow WBC. Figure 11 shows averaged over 1390 days (3.8 years) relative vorticity pattern with streamlines on it. The method of streamline calculation is described in the Appendix A1. Although viscosity in this experiment is relatively small  $A_M = 100 \text{ m}^2 \text{ s}^{-1}$  and the wind stress as for all other experiments is  $\tau = 0.3 \text{ Pa}$ , the system still reaches a steady state after the spin up time.

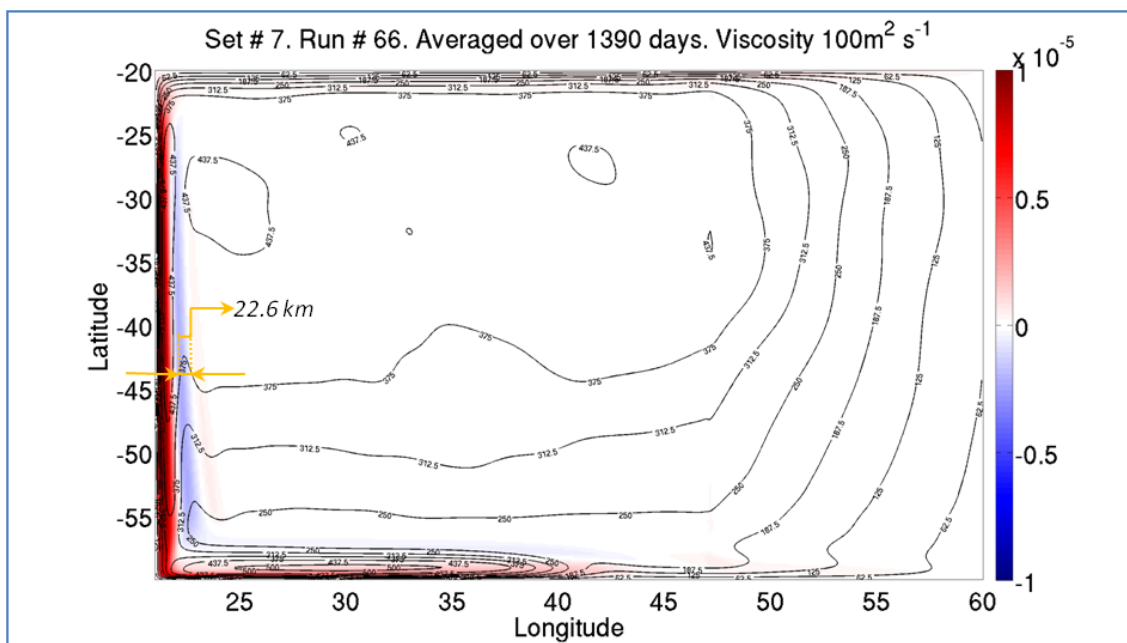


Figure 11. Averaged over 1390 days relative vorticity pattern with streamlines on it. The viscosity in this experiment is  $100 \text{ m}^2 \text{ s}^{-1}$ . Colors indicate relative vorticity within the scale range between  $-10^{-5}$  and  $10^{-5} \text{ s}^{-1}$ . Contours represent streamlines, which are calculated according to the method described in the Appendix A1. Contour interval is  $62.5 \text{ m}^2/\text{s}$ .

From Figure 11 it is seen that there are meanders at the south along with two recirculation areas: near the western boundary and at the south. This flow structure seems quite similar to the numerical experiment of inertial currents in the presence of friction for large Reynolds number,  $Re = 60$  ( $Re = \frac{UL}{A_M}$ , where  $L$  – characteristic scale for horizontal scale of the motion, other variables are defined above) described in Pedlosky (1986). However, there is a main difference in the wind forcing between our experiment and the one in Pedlosky, who used a sinusoidal wind forcing over the whole domain. Thus, in our experiment no eastward flow is prescribed along the WBC, because there is no forcing for that; but it is still happening.

Moreover, besides the similarity of the qualitative picture, some characteristics of the observed flow in a rectangular domain experiment are alike to the theory of the inertial currents in the presence of friction.

In this way, according to the theory, the number of oscillations in the southwestern part of the basin (Figure 11) before decay is  $O((\delta_i / \delta_m)^3)$ . In the experimental case

$$\delta_m = \left( \frac{A_M}{\beta_0} \right)^{1/3} = \left( \frac{100 m^2 s^{-1}}{1.87 \cdot 10^{-11} m^{-1} s^{-1}} \right)^{1/3} = 17.5 km \quad (1.10)$$

$$\delta_i = \left( \frac{V}{\beta_0} \right)^{1/2} = \left( \frac{0.01 m s^{-1}}{1.87 \cdot 10^{-11} m^{-1} s^{-1}} \right)^{1/2} = 23.1 km \quad (1.11)$$

where  $\delta_m$  - length of Munk boundary layer,  $\delta_i$  - length of inertial boundary layer,  $V$  is Sverdrup velocity for this experiment, and the reference latitude for calculation of  $\beta_0$  is  $\varphi = 35^\circ S$ .

Hence, there should be around 2 oscillations before the streamlines level off at the south and it is around 2 full oscillations in this rectangular domain experiment. Also the length scale of meandering is similar to  $\delta_i$  which corresponds to the theory as well (Figure 11).

In the theory, the behavior of the inertial flow in the presence of friction is explained by the structure of zonal velocity pattern within the WBL. It is known that purely inertial current is possible only for an area where zonal velocity is negative ( $u < 0$ ). Once it becomes positive ( $u > 0$ ) the standing Rossby waves appears, whose existence invalidated the purely inertial theory; however, in the presence of friction they are possible and are slowly damped as shown above. Figure 12a) demonstrates the averaged in time zonal velocity pattern for our rectangular domain experiment,

which again shows the similarity with the theory: starting from the latitude where zonal velocity changes sign (30-35°S), oscillations emerge (Figure 12b), Figure 12c).

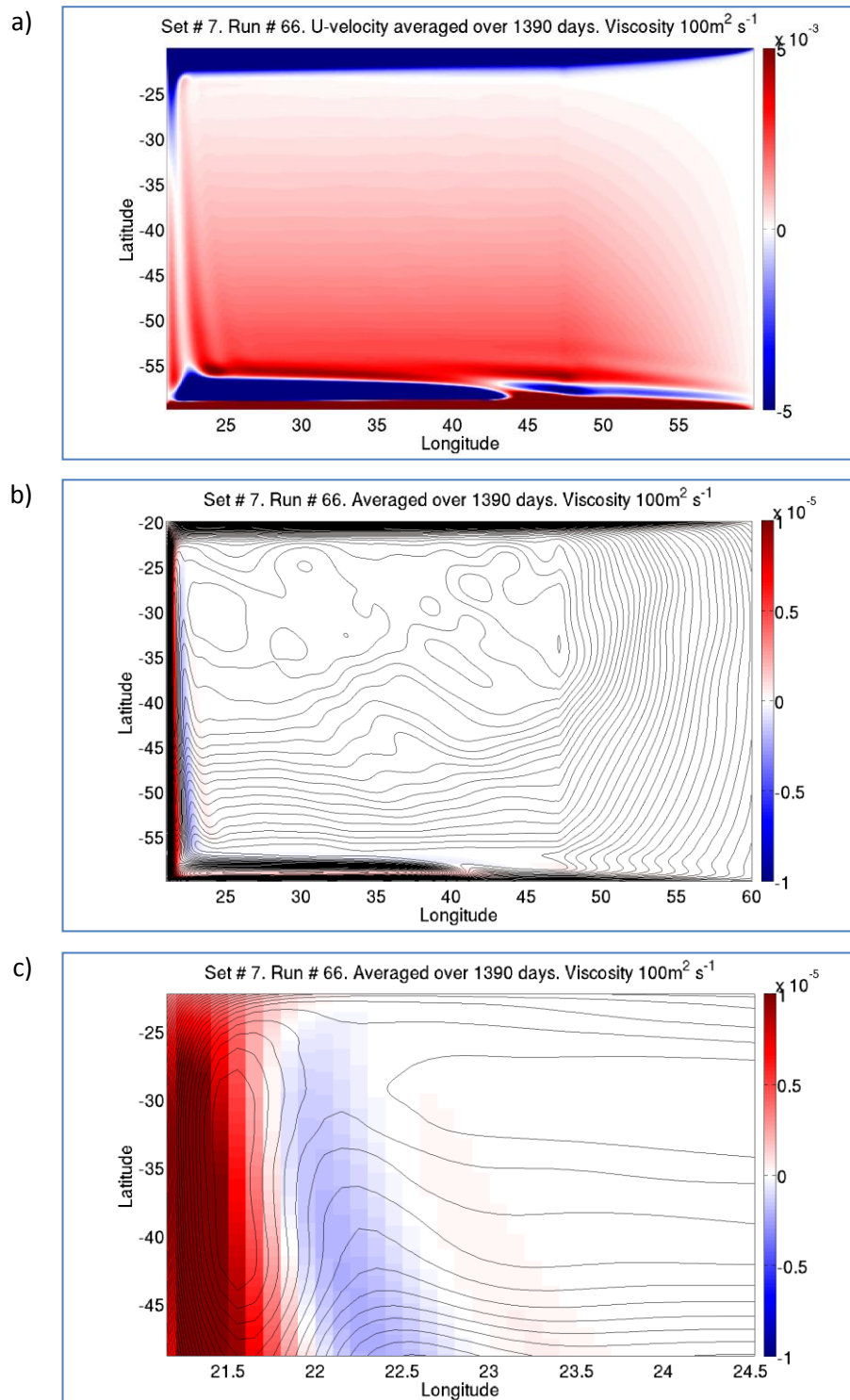


Figure 12. a) Averaged over 1390 days zonal velocity pattern. Top view of the domain. The colors are saturates to the limits  $\pm 5 \cdot 10^{-3} \text{ms}^{-1}$ ; b) Relative vorticity with streamlines on it. Colors indicate relative vorticity within the scale range between  $-10^{-5}$  and  $10^{-5} \text{s}^{-1}$ ; c) Zoomed in version of previous panel.

## 5.3.Southern tips

### 5.3.1. Separation at the south of Madagascar

The first set of experiments (Figure 8a) is intended to model the situation south of Madagascar and detect a different behavior of the flow between slip and no-slip boundary lateral conditions at the WBL separation and subsequent dipole formation.

Two sets of sensitivity experiments with various values of viscosities under slip and no-slip BC are presented in Figure 13 and Figure 14. The general circulation for slip and no-slip experimental sets fits the Sverdrup theory. The northward Sverdrup flow is balanced by the narrow WBL at the east of the continent, which subsequently propagates westward until the domain boundary and finally joins the interior via south, moving along the southern boundary. This general structure of the flow is similar for the slip and no-slip experiments.

For the no-slip experiments, it is seen that for the whole range of viscosities the separation is very pronounced and is at the southern tip in the form of dipoles. The orientation of the dipole centerline is preferably southwest-northeast for high values of viscosity and northwest-southeast for the viscosity of the order of  $100m^2s^{-1}$ . Note that the separation point does not change its position at different viscosities.

The streamlines on Figure 13 wiggles within the interior of the basin while making Sverdrup circulation. The irregularity becomes more striking when viscosity decreases. That is likely a result of additional Rossby waves that are excited by local variability from the zonal jet, which occurs after separation and also by perturbations along domain boundaries (LaCasce and Isachsen, 2007).

As for the slip set, the Sverdrup flow is clearer than for the no-slip case and the interior streamlines are directed almost northward. However the separation is not in the form of dipoles here, instead, the jet meanders to the west after passing the southern tip. The length scale of meanders depends on the viscosity and decreases when viscosity goes down. Besides, the meandering structure is very regular and is in the staggered order.

With the  $100m^2s^{-1}$  viscosity the current from the WBL wraps the continent and detaches from the land only after a substantial trip to the north (Figure 14e). The detachment happens only when the alongshore velocity becomes zero. To verify this statement, eastern and western sections just after the land (first sea grid points) were chosen, shown in Figure 15 by green lines. The position of separation in this experiment at  $37^\circ S$  exactly coincides with the position when the meridional velocity changes sign (Figure 16b).

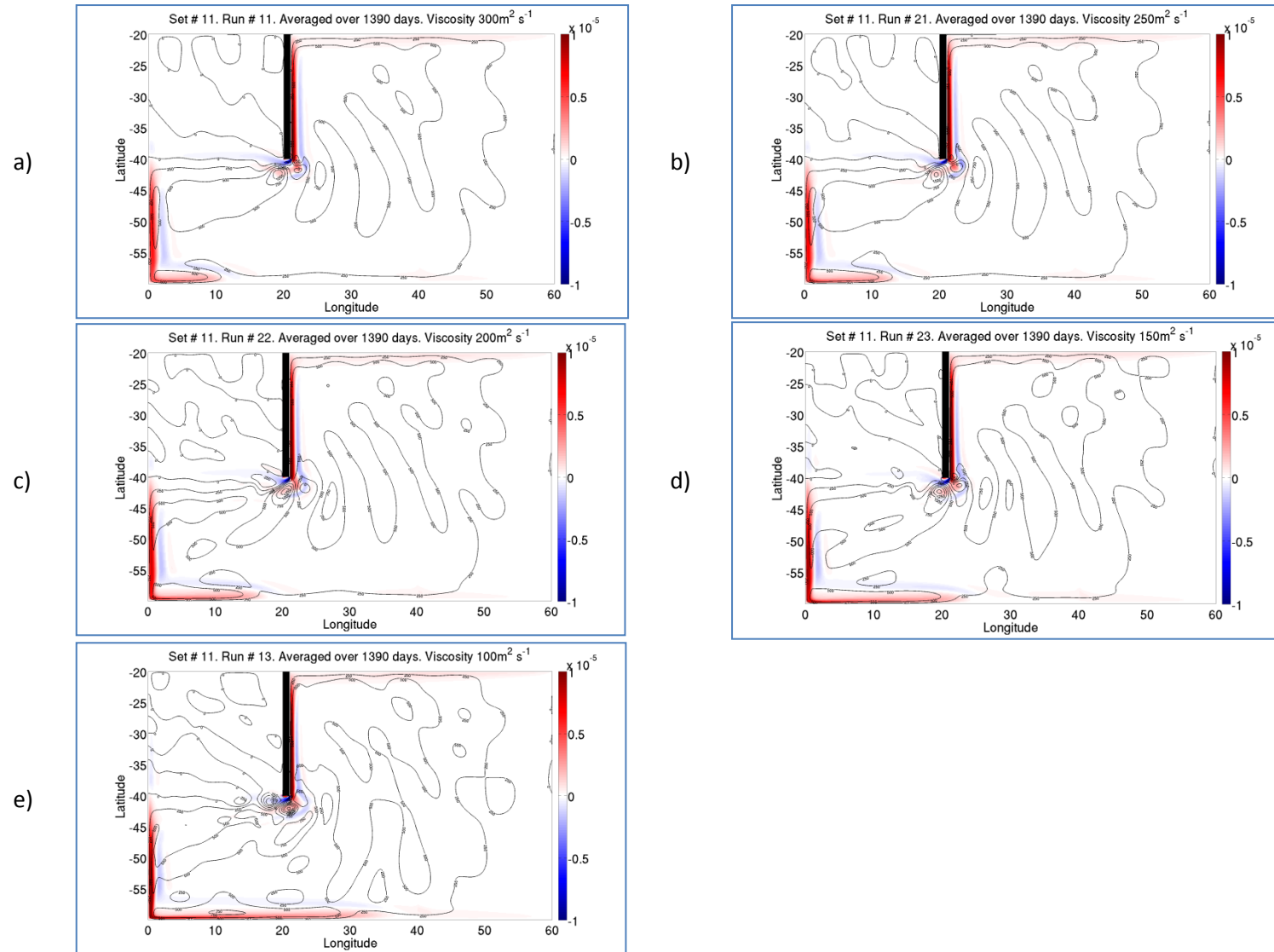


Figure 13. Same as Figure 11. Black 1° rectangle - land. The viscosity changes from 300 to 100 m<sup>2</sup>s<sup>-1</sup> from a) to e). No-slip BC.

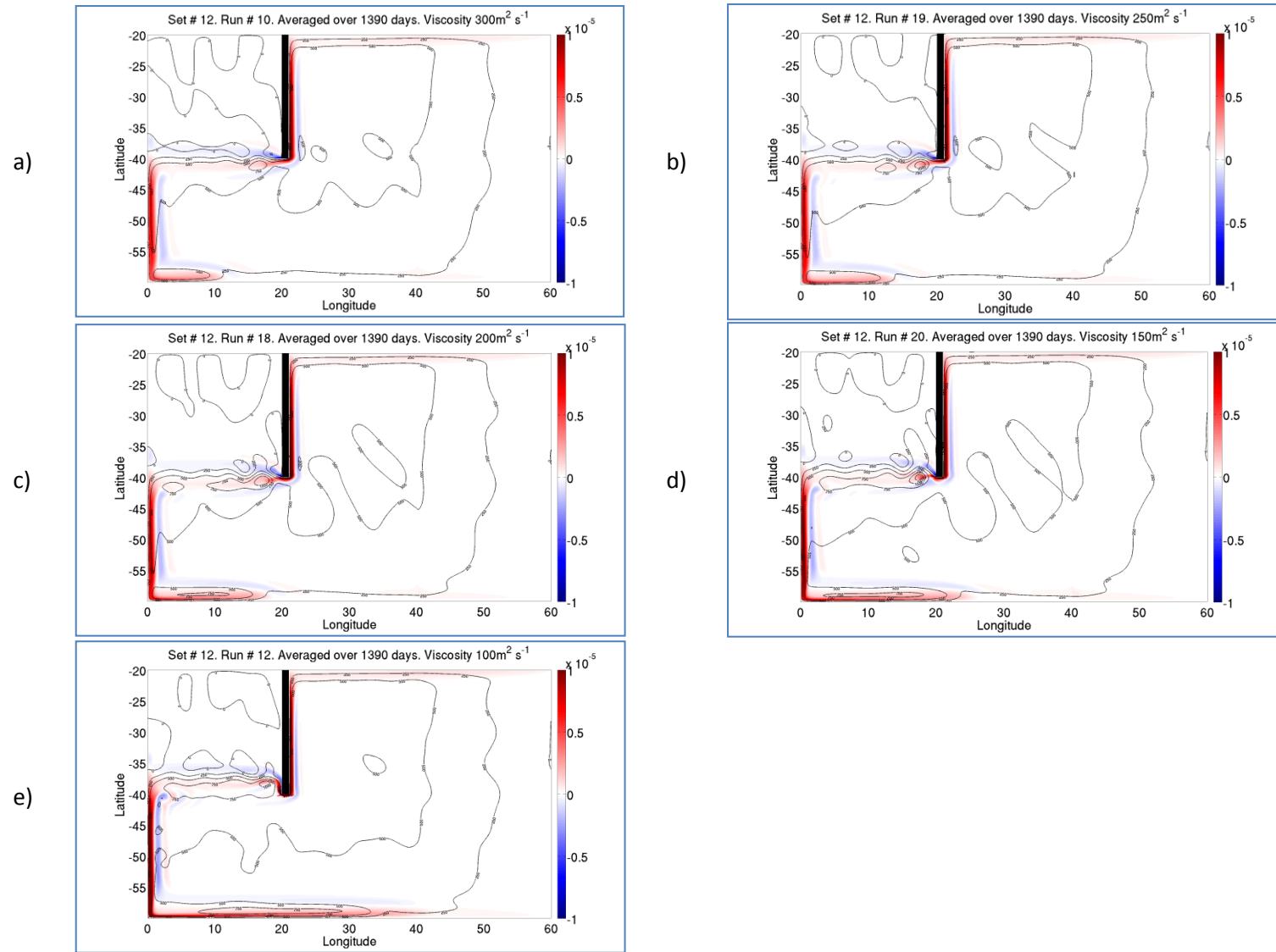


Figure 14. Same as Figure 13. Slip BC.

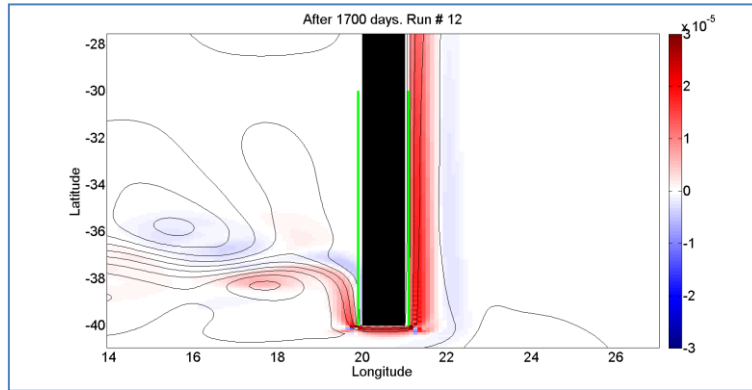


Figure 15. Example of relative vorticity pattern after 1700 model days. Other description is same as in Figure 11. Green lines - sections on the first sea grid points for verification of the meridional velocity structure. Experiment: slip, viscosity  $100\text{m}^2\text{s}^{-1}$ .

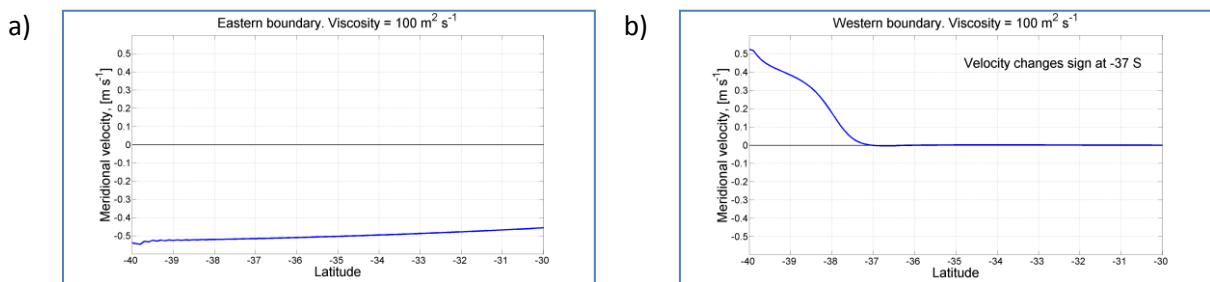


Figure 16. Meridional velocity profile along two sections: a) eastern, b) western. Positive values mean the direction from the south to the north, negative – vice versa.

### 5.3.1.1. Explanation of the different behavior at separation for slip and no-slip conditions.

Dengg (1992) shows that with slip boundary configuration the separation at the sharp corner does not occur, instead the flow wraps the continent and follows the boundary until it reaches the necessary PV that allows leaving the boundary layer.

To understand this different behavior at separation, consider two streamlines: the first forms the recirculation cell after separation ( $S_1$ ), the other one separates at the tip and has southwest orientation ( $S_2$ ) (Figure 17).

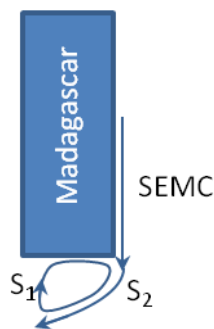


Figure 17. Schematic separation of the WBL. No-slip case.  $S_1$  – the streamline of the recirculation cell after separation.  $S_2$  – the streamline that joins the Sverdrup flow after separation.

Evaluating the integration of barotropic vorticity equation (1.1), we left out only the one term, since there is no wind at this region of the domain and the planetary vorticity and the advection terms do not contribute to the balance when integrated around a closed gyre.

$$A_H \oint_{\psi} (\vec{\nabla} \zeta \cdot \vec{n}) dl = 0 \quad (1.12)$$

In order to have a balance (1.12) for a closed streamline  $S_1$ , the relative vorticity along this streamline must consist of two parts: negative and positive. Inside the boundary layer in the north, positive vorticity due to no-slip BC is generated. Therefore, the only supply of negative vorticity is the streamline  $S_2$ . For the no-slip it is not a problem since, in this case, the WBL has negative relative vorticity on the coastal flank (frictional sublayer) which may be advected by the nonlinear term and subsequently diffused into the  $S_1$ . However, the WBL under slip conditions does not have source of negative vorticity, therefore the recirculation cell  $S_1$  cannot exist. Thus, since the slip stream is not able to supply the negative vorticity into the 'lee' side of the expected separation position, then it cannot separate and the only variant is to turn the corner and follow the coast.

### 5.3.1.2. Determination of meander period and wave period. Slip BC

As it was described in section 5.3.1 the meandering of the westward jet after passing the southern tip is regular in time. The period of such regular structure might be correlated with the period of the basin modes.

Consider one 10-day averaged relative vorticity pattern that corresponds to  $350 \text{ m}^2\text{s}^{-1}$  viscosity and slip BC after 5 model years of simulation (Figure 18).

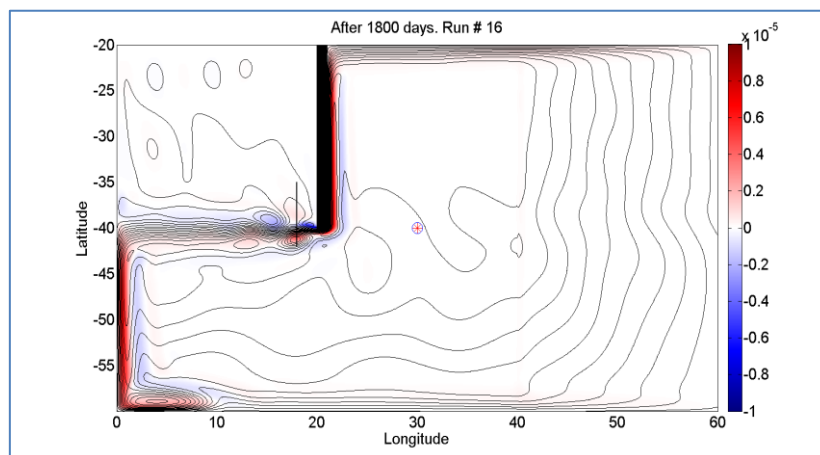


Figure 18. Example of relative vorticity pattern after 5 model years. The viscosity in this experiment is  $350 \text{ m}^2\text{s}^{-1}$ . Contours represent streamlines, which are calculated according to the method described in the Appendix A1. Black rectangle –  $1^\circ$  land, thin black line – section for determination of an eddy appearance period. Red-blue point at  $(30^\circ\text{E}, 40^\circ\text{S})$  – the point for determination a wave period.

According to the results of experiments under slip BC (Figure 14), all generated eddies propagate to the west trough the section along 18°E between 35°S and 42°S (black line on Figure 18), therefore such a section was chosen to determine an eddy appearance period. For each time step, which is equal to 10 days in this case, the sum of relative vorticity along the section is recorded (red dots on Figure 19).

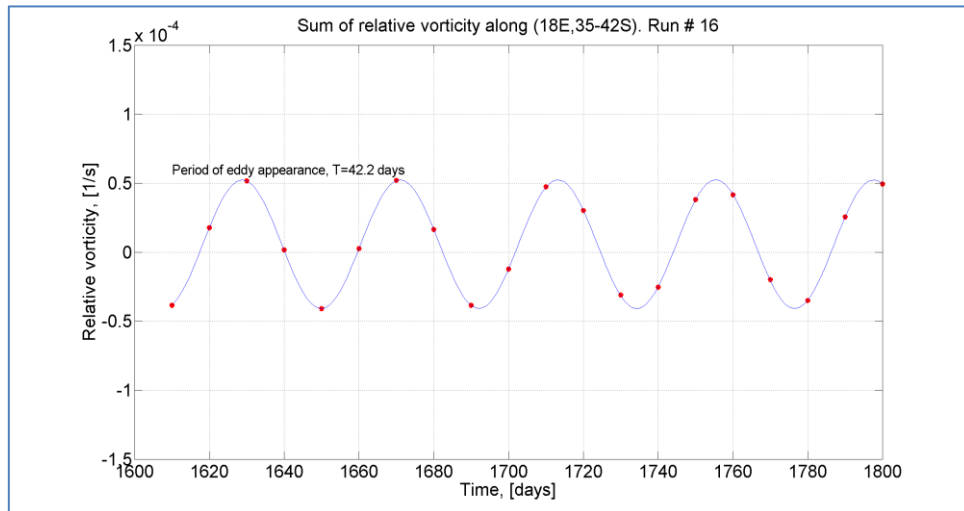


Figure 19. Nonlinear regression analysis to determine eddy appearance period. Red dots – actual values of relative vorticity sum along section (18°E, 35°S – 42°S). Blue line – reconstructed time dependence.

Then, a nonlinear regression analysis is performed to reveal the period. In the example case, the period of eddy appearance is 42.2 days.

For the calculation of a main basin wave period, the method is almost the same, but instead of the section, a single point (30°E, 40°S) is selected, and instead of relative vorticity - sea surface height is analyzed.

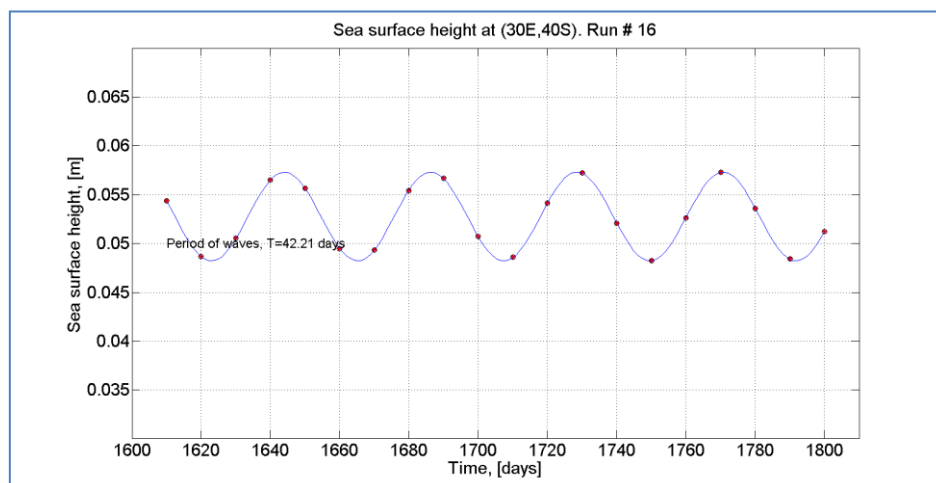


Figure 20. Nonlinear regression analysis to determine main basin wave period. Red dots – actual values of sea surface height at the positions (30°E, 40°S). Blue line – reconstructed time dependence.

The period of basin modes for this example is 42.21 days; that is almost identical to the eddy appearance period. This analysis was carried out for the whole range of viscosities; the result is presented in Figure 21. From this graph, it is clear that the eddy period is in high correlation with the period of basin modes.

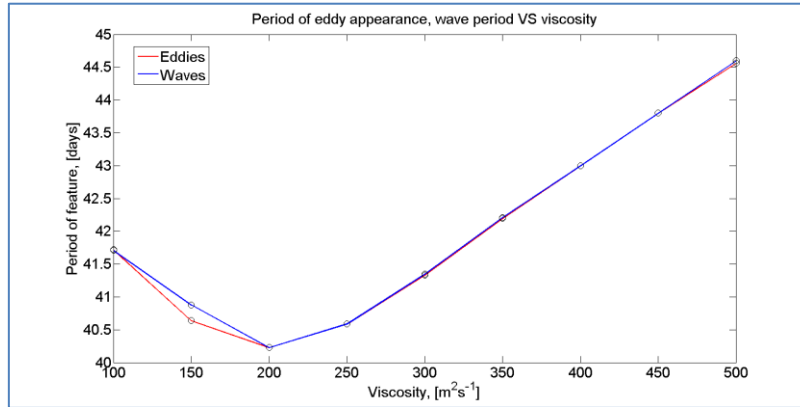


Figure 21. Dependence of eddy appearance period and main basin wave period on viscosity. Slip BC. Red line correspond to eddies, blue to basin modes.

However, it is hard to say what influences each other; either basin modes control the generation of meanders or meanders influence the wave production.

In order to explain this dependence the following hypothesis is proposed. It is assumed that the source for the basin modes is barotropic instability along the domain boundaries; especially when the flow reaches the northern boundary and starts propagating westward along the northern domain boundary. In Appendix A2 it is shown that shear flow (of the specific structure as in Figure 42) may encourage the development and propagation of waves from small initial perturbation. It is also shown that the wavelength of the fastest growing perturbation ( $\lambda$ ) that dominates the early stage of instability and probably remains after development, is about eight times the width of the shear zone ( $L$ ). In slip case the velocity profile at the northeast of the domain is shown in Figure 22, so here we deal with shear flow, which has a similar structure as in Figure 42.

If assume that exited waves are Rossby waves propagating in the zonal direction, then the dispersion

relation is  $\omega = -\beta_0 R^2 \frac{k_x}{1 + R^2 k_x^2}$ , where  $k_x$  - wavenumber ( $k_x < 0$ ),  $R = \frac{\sqrt{gH_0}}{f}$  - Rossby radius of

deformation. Hence, period of waves is

$$T = \frac{2\pi}{\omega} = -\frac{2\pi}{\beta_0 R^2} \frac{1 + R^2 k_x^2}{k_x} = \frac{2\pi}{\beta_0 R^2} \frac{1 + 4\pi^2 R^2 / \lambda^2}{2\pi R^2 / \lambda} = \frac{1}{\beta_0 R^2} \frac{1 + 4\pi^2 R^2 / (8L)^2}{R^2 / (8L)} \propto \alpha L + \frac{\gamma}{L},$$

where  $\alpha$ ,  $\gamma$  - constants.

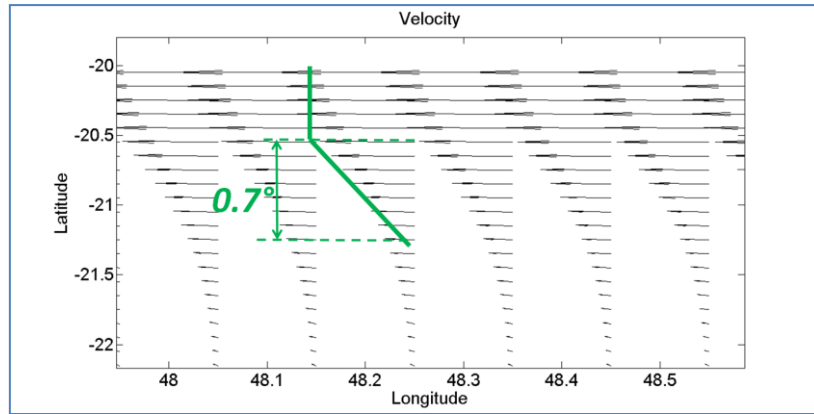


Figure 22. Qualitative picture of the velocity structure at the northeast of the domain during spin up time. Green line – approximation of such profile. Example of slip experiment with viscosity  $350\text{m}^2\text{s}^{-1}$ .

In Figure 22 the width of the shear zone is around  $0.6 - 0.7^\circ$ . If this value is substituted into the formula for wave period, it gives approximately 43 days. This number correlates well with wave periods that were found for basin modes.

Moreover, it is evident from Figure 21 that wave period depends on viscosity. Intuitively, it may happen because when viscosity decreases the length of the shear zone increases and vice versa. If it is assumed that the length of the shear zone and viscosity are inversely proportional quantities (

$$LA_M = 1), \text{ then the period depends on viscosity as } T \propto \frac{\alpha}{A_M} + \gamma A_M.$$

The graph of this function when constant coefficients are set to zero is presented in Figure 23.

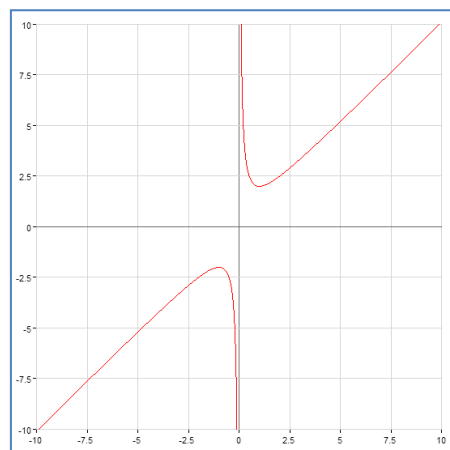


Figure 23. The graph of function  $y=x+1/x$ .

Thus, when viscosity is large, wave period increases linearly with viscosity, but when viscosity is small and beyond a certain threshold, wave period behaves as a hyperbolic function. It nicely agrees with the dependence which we got from slip experiments.

### ***5.3.1.3. Determination of eddy period and wave period. No-slip BC***

Determination of wave period and eddy period for the no-slip case is more difficult than in section 5.3.1.2 for slip experiments, because there is more time variability in the no-slip and the propagation of eddies is more irregular.

In Figure 13 it is seen that either waves in the main basin influence the eddy generation or eddies play a role in producing waves. The velocity structure at the northern boundary for the no-slip condition is similar to slip case (Figure 22); because the frictional sublayer is not explicitly resolved by the model, instead, 'ghost' velocity point is set on the other side of the boundary (Section 3.2). Therefore, based on the discussion above it is likely that waves control eddy appearance period in no-slip experiments too.

Looking at the 10-day averaged snapshots (Figure 24), it is clear that there is some variability in the WBL that propagates upstream. To determine the period of these variations and an eddy separation period, three sections (diagonal, zonal #1 at 35°S and zonal #2 at 30°S) and one point at (40°E; 40°S) are chosen (Figure 25). For each section the summation of relative vorticity is calculated and recorded for each time step. Afterwards, the approximate periods are defined (Figure 26).

The period of eddies (Figure 26a) is around 40 days, which is quite the same as the wave periods in the main basin (Figure 26d). As for perturbation in the WBL, its period is also of the order of 40-45 days. This analysis indicates that all features: eddies, waves, WBL disturbances are connected to each other; however what the primary cause is, is still difficult to say.

$\nu = 100$  . No-slip BC.

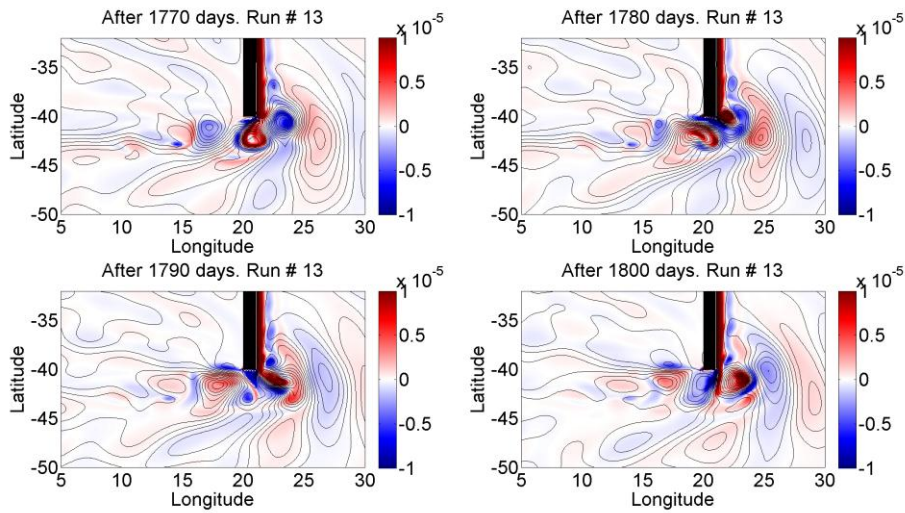


Figure 24. Time series of 10-day averaged relative vorticity patterns. Experiments with no-slip BC. Viscosity is  $100 \text{ m}^2 \text{ s}^{-1}$ . Colors indicate relative vorticity within the scale range between  $-10^{-5}$  and  $10^{-5} \text{ s}^{-1}$ . Contours represent streamlines, which are calculated according to the method described in the Appendix A1.

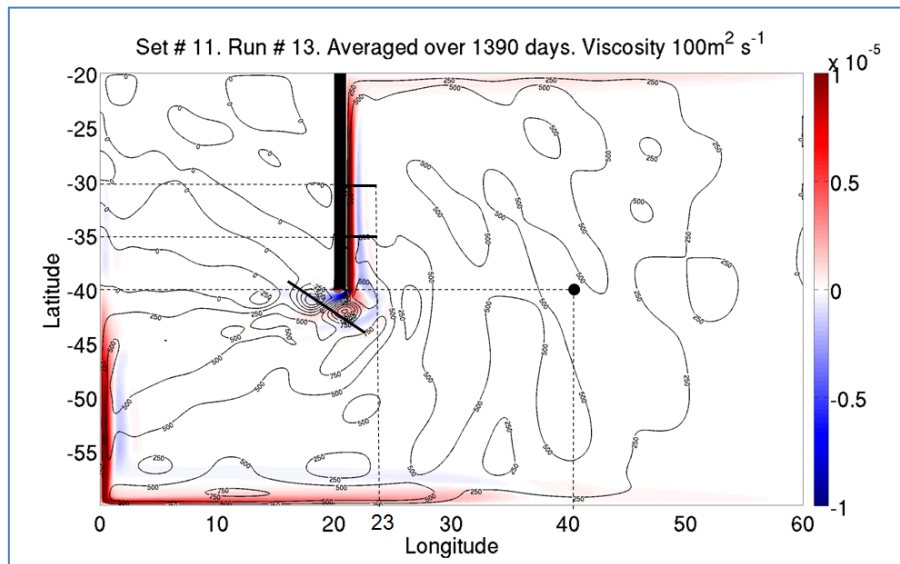
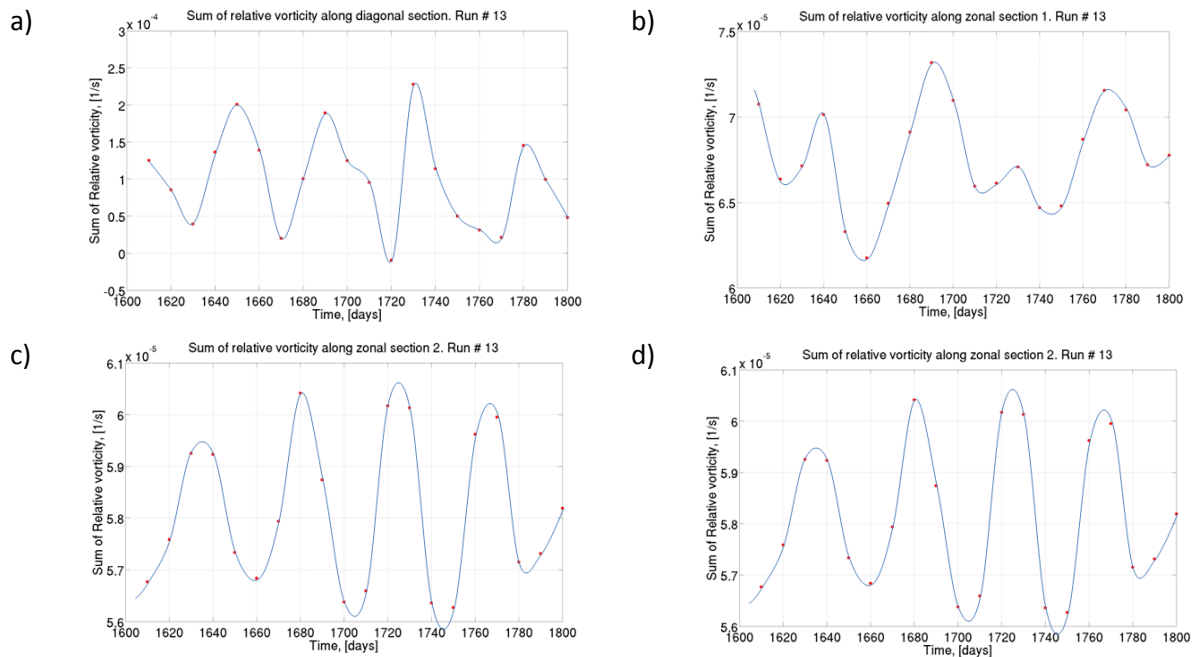


Figure 25. Same as Figure 13. The viscosity is  $100 \text{ m}^2 \text{ s}^{-1}$ . Thin black lines – sections for determination of an eddy appearance period and WBL disturbances. Black point at  $(40^\circ\text{E}; 40^\circ\text{S})$  – the point for determination a wave period.



**Figure 26. Analysis for determination of a) period of eddy appearance and, b)-c) period of WBL disturbances, d) period of main basin wave period. Red dots – actual values. Blue line – reconstructed time dependence.**

Figure 26 also gives an information about a phase difference in signals of the first section (21°E-23°E,35°S) and the second section (21°E-23°E,30°S) which means that the propagation speed of the disturbance that goes upstream is around

$$c = \frac{5^\circ}{30h} = \frac{555km}{30h} = 15.85kmh^{-1} = 4.4ms^{-1}.$$

#### 5.3.1.4. Integral characteristic. Slip and no-slip

In order to investigate the behavior of the relative vorticity field while flow moves along the western boundary and then propagates westward, two sections: zonal and meridional, were selected. The zonal section from 21°E until 25°E at latitude 35°S covers the whole boundary current, and the meridional section extends from 33°S to 48°S at longitude 18°E across the pathway of the dipole propagation and the westward jet taking into account all experiments: slip and no-slip.

The formula used for integration along the zonal section is

$$J = \int_{x=21^\circ E}^{x=25^\circ E} \zeta_{ij} dx = \int_{x=21^\circ}^{x=21.05^\circ} \zeta_{ij} dx + \int_{x=21.05^\circ}^{x=25^\circ E} \zeta_{ij} dx \quad (1.13)$$

where  $dx = a \cos \theta_j \Delta \phi$ ,  $a$  – radius of the Earth,  $\Delta \phi$  - meridional spatial step,  $(i, j)$  - position on the grid. The formula (1.13) has two terms because of the implementation of boundary conditions that was discussed in section 3.2. Thus, for the boundary point at 21°E only half a grid length should be taken for integration.

The formula for along meridional section is

$$J = \int_{y=45^{\circ}\text{S}}^{y=33^{\circ}\text{S}} \zeta_{ij} dy \quad (1.14)$$

where  $dy = a\Delta\theta$ ,  $\Delta\theta$  - zonal spatial step.

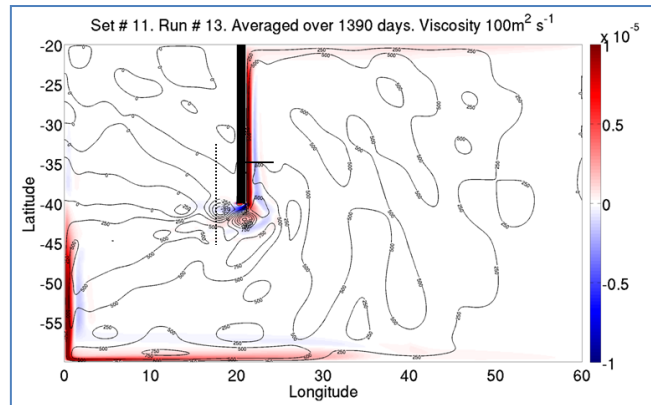


Figure 27. Same as Figure 13. Solid black line - zonal section (21-25°E,35°S). Dashed line - meridional section (18°E,33-48°S). No-slip experiment with  $100 \text{ m}^2 \text{ s}^{-1}$  viscosity is taken as an example for a background.

The integration was performed for each experiment (Figure 13, Figure 14) for each time step and then averaged over 1390 days. Then, the integral value is normalized on the length of the section.

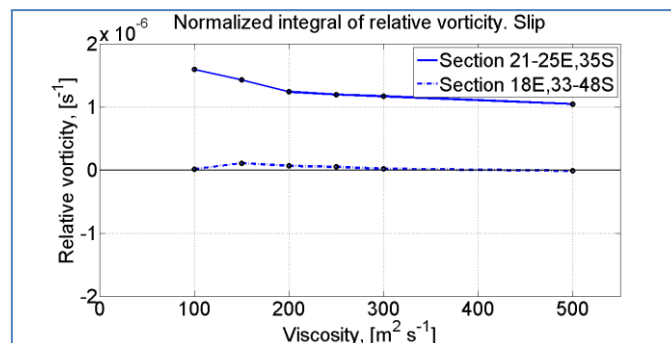


Figure 28. Normalized Integral of relative vorticity along zonal and meridional section for slip experiments.

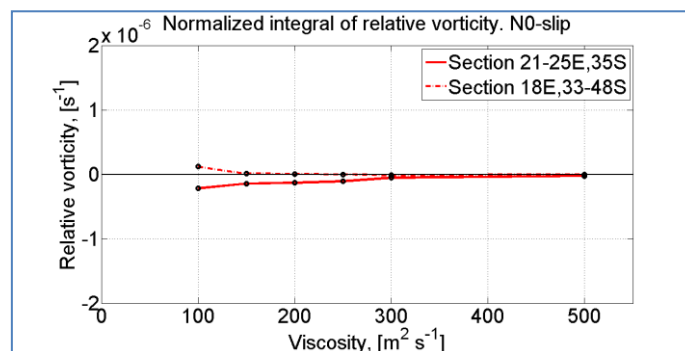


Figure 29. Integral of relative vorticity along zonal and meridional section for no-slip experiments.

Figure 29 shows that under high values of viscosity in the no-slip experiments the normalized integrals along two sections coincide with each other and are almost zero. It is indeed what was expected – the flow has zero net relative vorticity across the WBL (Stewart constraint, 1989) and while propagating westward after separation it retains this same value. By decreasing the value of viscosity some difference happens. The total relative vorticity along the zonal section shifts to the negative side whereas the total relative vorticity along the meridional section becomes positive. It could be because, under small values of viscosity some perturbations with cyclonic behavior (negative vorticity) are generated and dragged upstream, and the WBC after some movement to the south (Figure 24). Therefore this disturbance might be counted as an extra negative source to the net relative vorticity along the zonal section. At the same time the remaining flow contains total positive relative vorticity after these perturbations have detached from it, which means that there is a positive net relative vorticity along the meridional section. Based on this explanation, the absolute values of the net relative vorticity along both sections should be the same. From the figure above it is seen that a divergence of lines is indeed quite symmetric.

With respect to slip experiments (Figure 28), the total relative vorticity along the zonal section is positive because there is no source of the negative vorticity due to absence of the lateral friction. After separation and propagation to the west, the flow is organized in a way that the averaged total relative vorticity is about zero. It is because once the flow leaves the shore of the island it has achieved the necessary PV to join the interior. The necessary PV is reached because of the loss of anomalously high values of relative vorticity that the flow had in the WBL, e.g. due to northward propagation after wrapping the island. Therefore, downstream from the separation there is no relative vorticity that originated from the WBL. However, once the separated jet starts propagating westward it suffers from the barotropic instability and starts meandering. These meanders are symmetrical and do not produce net relative vorticity if averaged in time. Also note, the separation takes place only when the alongshore velocity is zero. That could happen through momentum diffusion from the open ocean towards the shore.

Besides, the diagonal section (Figure 25) was treated with relative vorticity integration (only for the no-slip experiment with  $100 \text{ m}^2\text{s}^{-1}$  viscosity).

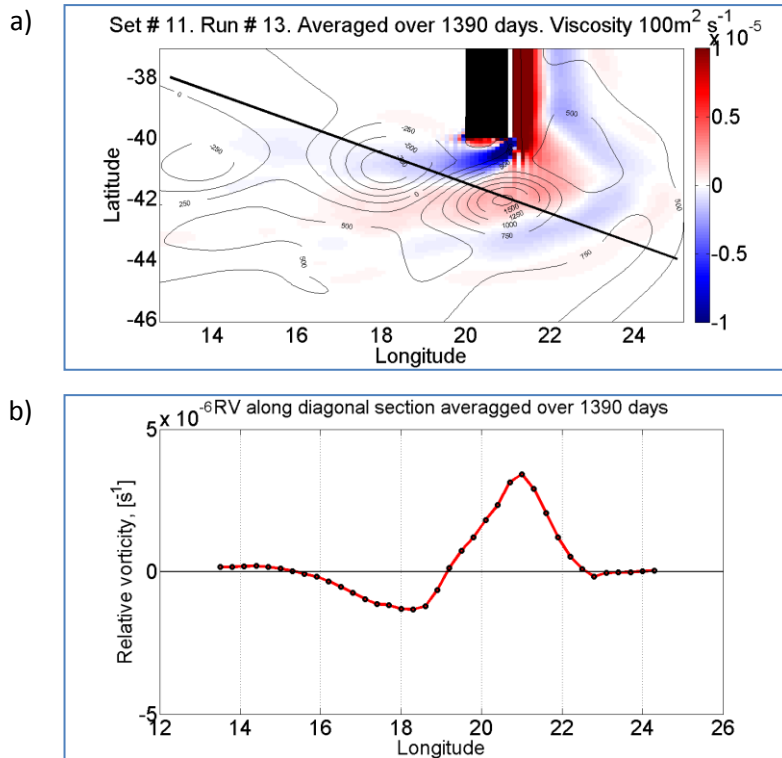


Figure 30. Same as Figure 13. a) Zonal section. b) Relative vorticity along the zonal section.

Figure 30b) indicates that the relative vorticity pattern is not perfectly symmetrical at the separation. The anticyclonic part is almost two times stronger than the cyclonic one. However, their length scale is similar and the diameter of each eddy is around 3 degrees. The normalized integral of relative vorticity along this section is  $3 \cdot 10^{-7} s^{-1}$ , which has the same order of magnitude as the normalized integral of relative vorticity along the meridional section  $10^{-7} s^{-1}$  (Figure 29,  $100 m^2 s^{-1}$  viscosity).

### 5.3.2. Agulhas retroflection

Use of the piecewise linear wind profile (Figure 8) shows the boundary current separation from the southern tip just as it does under no-slip BC in Figure 13. However, now the wind curl is applied only for the northern 25 degrees of the domain from  $20^{\circ}S$  till  $45^{\circ}S$ ; in the south from  $45^{\circ}S$  there is a uniform eastward wind. The meridional mass transport (the Sverdrup transport) is proportional to the curl of the wind stress, thus, if the curl is zero there is no transport and consequently there is a return current at  $45^{\circ}S$ , which is a subject for interaction with eddies. The sensitivity experiments with various viscosities (Figure 31) show that there is a bifurcation point at the separation and the flow at this position may go either to the west and subsequently join the interior with the return flow at  $45^{\circ}S$  or move directly to the east.

Also from this set of experiments a leakage to the western basin occurs. However, when it reaches the western domain boundary, this flow goes poleward until  $45^{\circ}S$  and then turns to the east in order to join the return current.

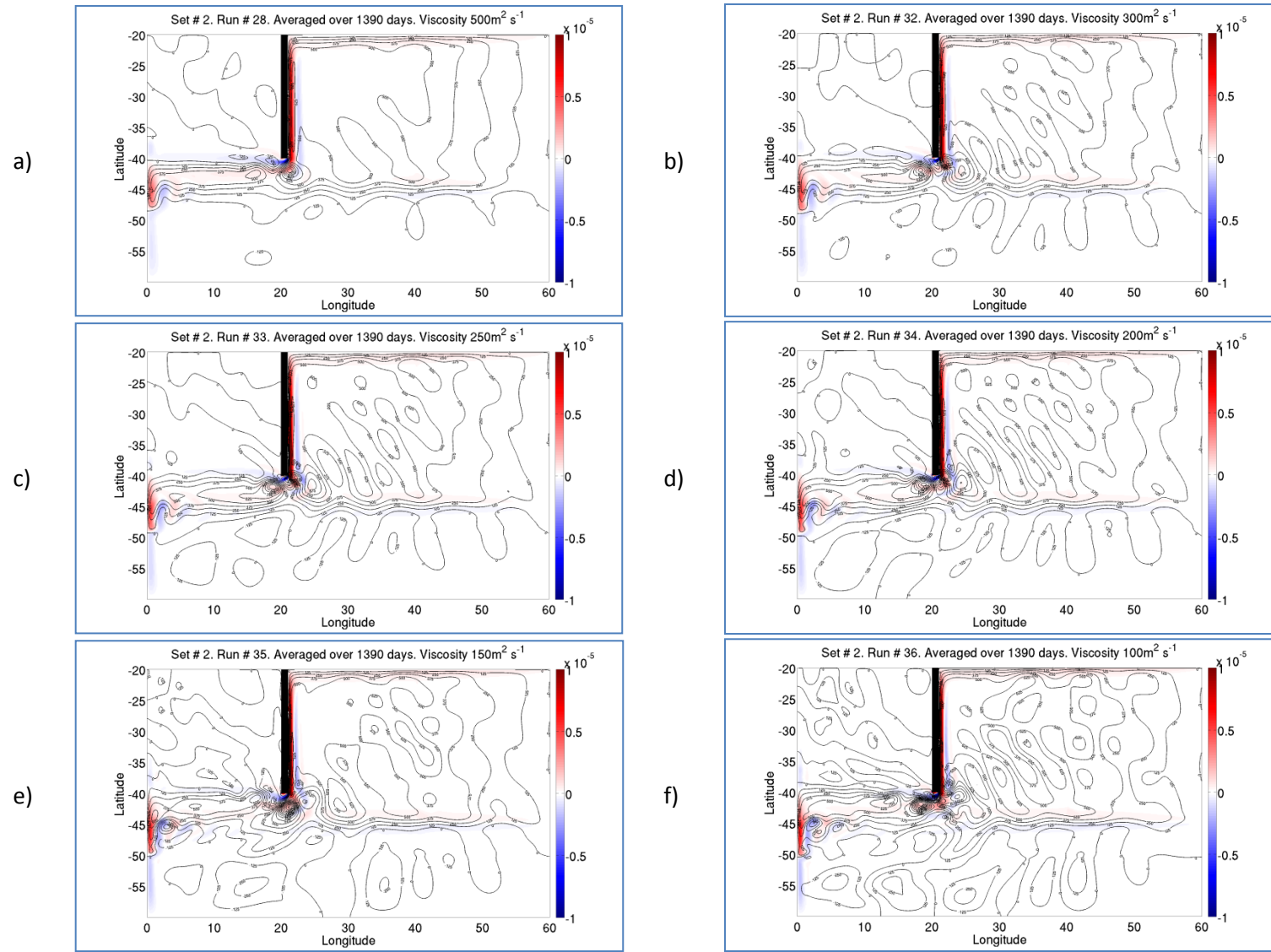


Figure 31. Experimental set # 2 – piecewise linear wind structure. Constant position of zero wind curl line. Other description is same as for Figure 13 but the viscosity range is a)  $500\text{ m}^2\text{ s}^{-1}$ , b)  $300\text{ m}^2\text{ s}^{-1}$ , c)  $250\text{ m}^2\text{ s}^{-1}$ , d)  $200\text{ m}^2\text{ s}^{-1}$ , e)  $150\text{ m}^2\text{ s}^{-1}$ , f)  $100\text{ m}^2\text{ s}^{-1}$ . No-slip.

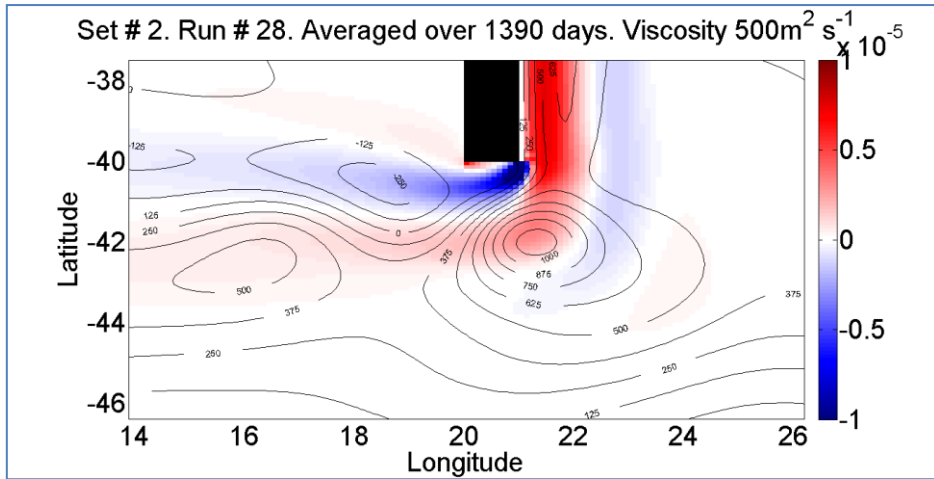


Figure 32. Experimental set # 2. Zoom-in version. Description same as Figure 13 but viscosity is  $500 \text{ m}^2 \text{ s}^{-1}$ .

Figure 32 shows this separation; streamlines with labels  $0$ ,  $125$ ,  $250$ ,  $375$ ,  $500$  belong to WBL, however after separation  $0$ ,  $125$ ,  $250$  go to the west, whereas  $375$  and  $500$  move to the east, making retroflection.

This experiment demonstrates that retroflection can be produced just with the use of appropriate wind forcing. This wind profile differs from the previous one only by the presence of the zero curl area and it dramatically changes the flow structure.

In order to estimate quantitatively (mass transport) a leakage from the WBL to the western basin, a zonal section within the WBL and a meridional section at  $5^\circ \text{E}$  across the leakage were chosen (Figure 33).

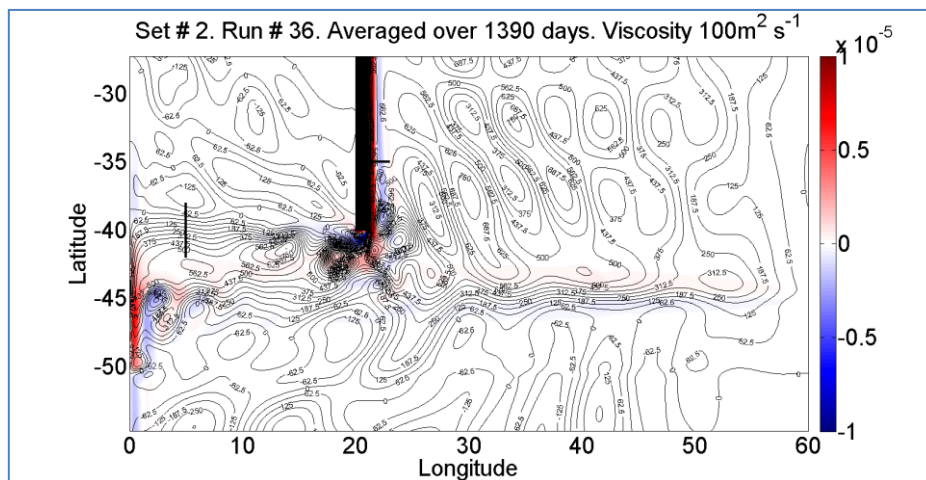


Figure 33. Experimental set # 2. Description same as Figure 13. Viscosity is  $100 \text{ m}^2 \text{ s}^{-1}$ . Black solid lines indicate sections for the estimation of leakage from the WBL to the western basin.

In Figure 31, it is seen that the leakage to the western basin is always within the latitude range 38°S and 42°S. Therefore the meridional section (5°E, 38°S - 42°S) is used for the whole experimental set # 2. The zonal section covers the WBL and is (21°E - 23°E, 35°S).

The percentage of the leakage (mass transport) for the set of viscosities is given in Figure 34. However, this result is far from the real situation, which is 10-20% of the inflow transport (de Ruijter et al., 1999), even when viscosity is  $100 \text{ m}^2\text{s}^{-1}$ .

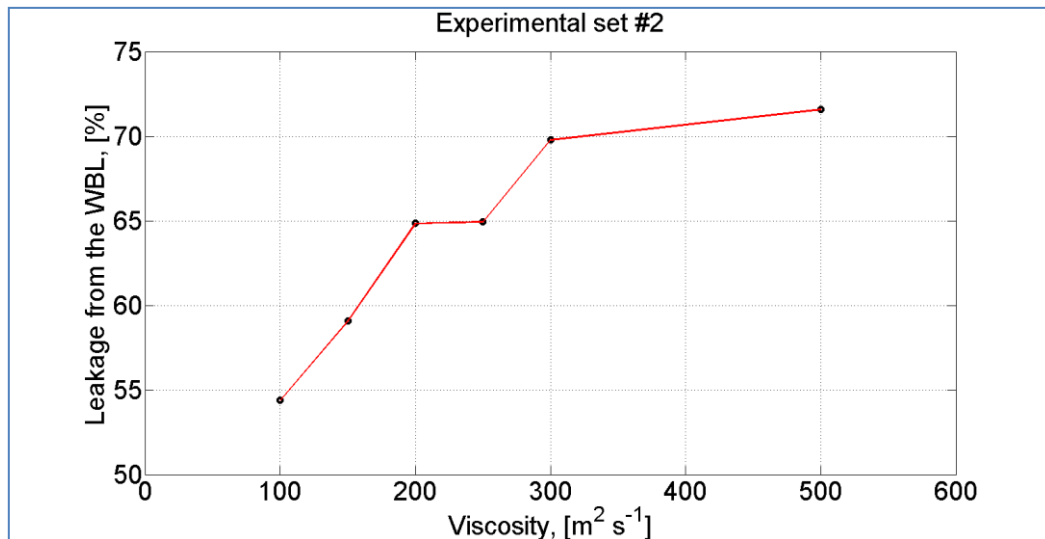


Figure 34. Dependence of leakage from the WBL to western basin in percentage from viscosity. Experimental set #2.

Other experiments within this framework were carried out with varying the zero wind curl position only for the viscosity of  $100 \text{ m}^2\text{s}^{-1}$ . Most of the experiments show the retroflection when the zero wind curl position lies in the vicinity of the southern tip, i.e. from 40°S to 43°S.

When wind curl ends at 40°S, it is seen from Figure 35f) that the WBC overshoots the southern tip for several degrees but then in order to recover PV the flow turns eastward and subsequently joins the eastward return flow that is at 40°S. By this, it produces the retroflection.

Similar separation happens when the wind curl stops at 41°S (Figure 35e), however the direction of overshooting is different. The stream from the WBC propagates southwestward until 12°E and afterwards makes a U-turn and follows the return flow.

The further to the north the zero wind curl line is located, the less streamlines from the WBC retroflect. The most pronounced retroflection is observed with the wind type where the zero wind curl line is at 41°S (Figure 35e).

The estimation of the leakage for this set of experiments is more complicated because there is no clear westward jet after separation that comes from the WBL.

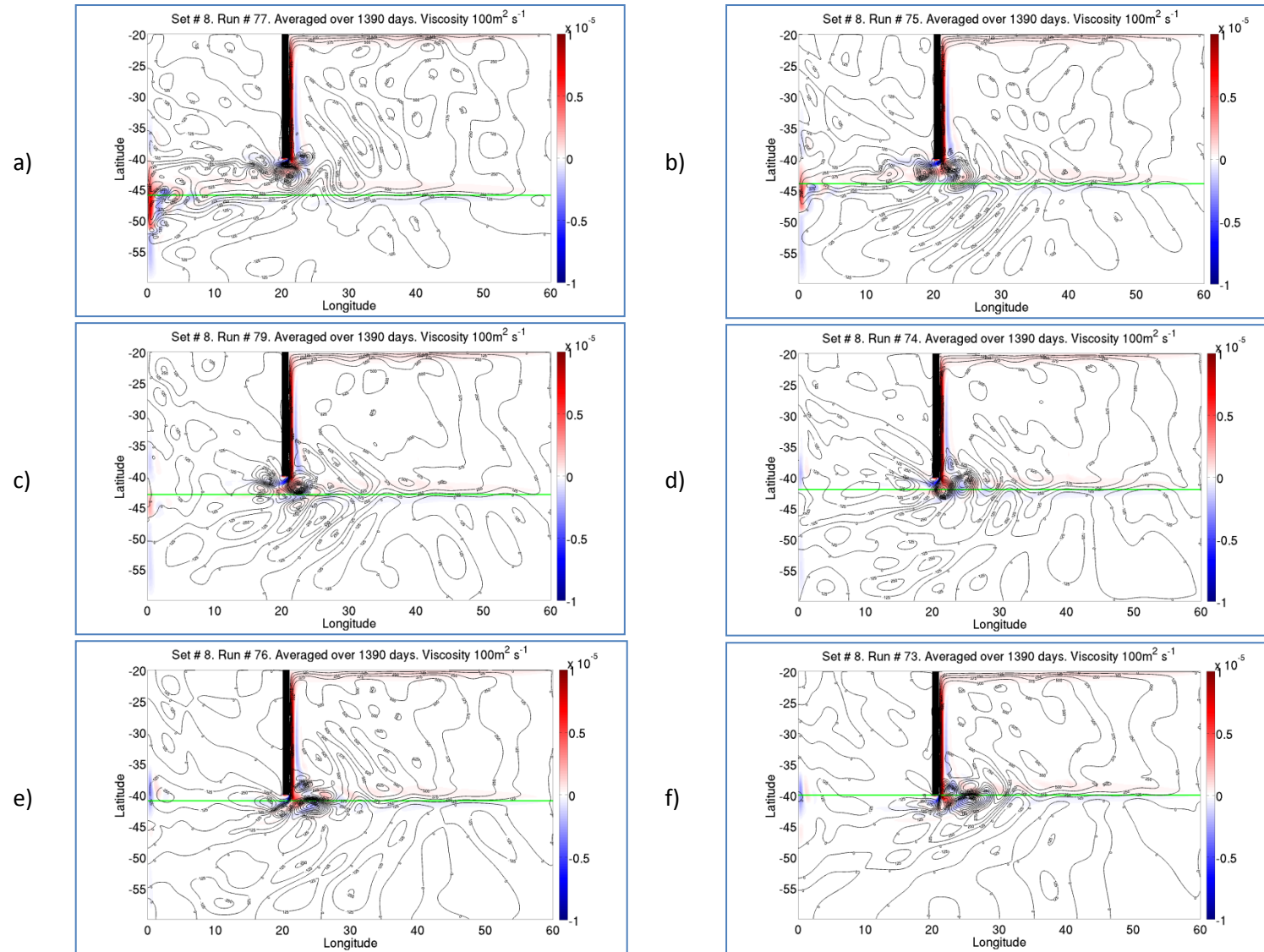


Figure 35. Experimental set # 2 – piecewise linear wind structure. Zero wind curl line varies and lies at a) 46°S, b) 44°S, c) 43°S, d) 42°S, e) 41°S, f) 40°S. Viscosity for all panels is  $100 \text{ m}^2 \text{ s}^{-1}$ . Other description is same as for Figure 13. No-slip.

The third set of experiments examines the separation within the framework of the two-gyre system, which is also relevant to the Agulhas separation. Such wind (Figure 8c) gives positive input of vorticity to the northern part of the domain and negative input for the southern part. Depending on the position where wind curl changes sign, the behavior of the flow differs. Here only one viscosity of  $100\text{m}^2\text{s}^{-1}$  is considered.

The return current – eastward jet that appears from both gyres located at the position of zero wind curl. This jet is meandering while propagating to the east. The general structure of separation under no-slip that was discussed in section 5.3.1.1 is observed here when the zero wind curl line lies far to the south from the separation area (Figure 37a). The generated eddies in this case are situated close to the return current, yet do not interact with it. When the zero wind line moves more to the north (Figure 37b), the generated eddies are caught by the eastward return current and form retroflexion. Further displacement of the zero wind line result in less pronounced retroflexion (Figure 37c); finally the WBL does not separate at the tip but immediately follows the meandering eastward jet (Figure 37d-e).

The retroflexion in the context of two gyres when the zero wind curl line is at  $44^\circ\text{S}$  (Figure 37b) is similar to the case where wind curl stops at  $41^\circ\text{S}$  (Figure 35e). In both cases most of the streamlines from the WBC change the southwestward course at around  $18^\circ\text{E}$ . The following movement depends on which latitude the return current passes.

The remarkable feature for these two sets of experiments is that the cyclone on the ‘lee’ side of the land is always formed (Figure 31, Figure 35, Figure 37). Sometimes it is accompanied with the anticyclone and forms a dipole pair. Figure 36 shows the situation where the dipole pair and the retroflexion are observed at the same time. The direction of this dipole is northwestward; such a flow pattern may refer to the Agulhas leakage to the Atlantic (De Ruijter et al., 1999).

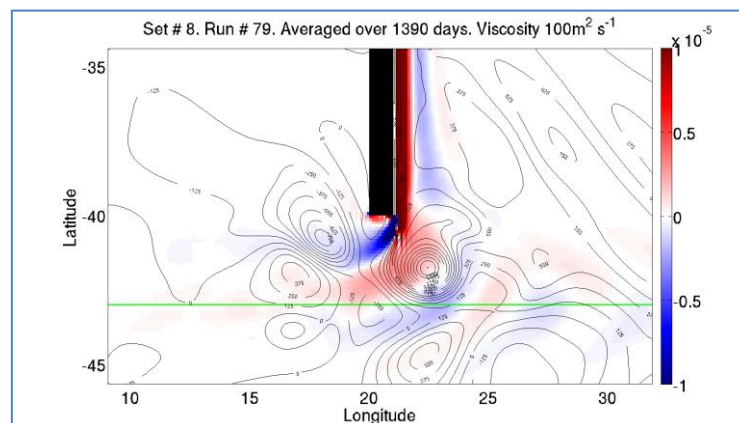


Figure 36. Same as Figure 35c) but zoomed in to the area of the separation.

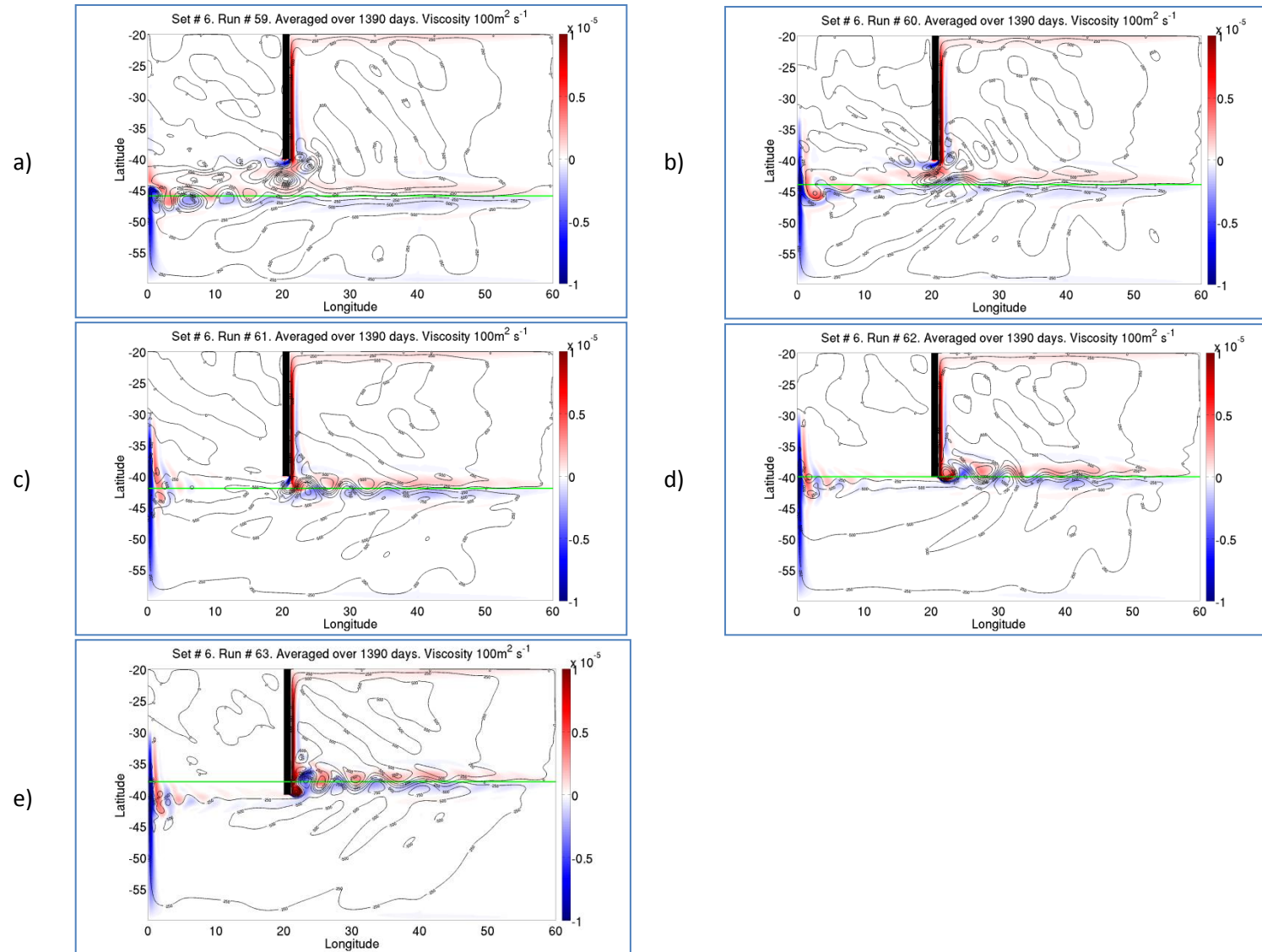


Figure 37. Experimental set # 3. Description is same as in Figure 13 but the viscosity is  $100\text{m}^2\text{s}^{-1}$  for all experiments. Zero wind curl position marked by green line. No-slip.

## 5.4. Northern tip of Madagascar

### 5.4.1. Linear wind profile

The experimental set # 4 simulates the case of one gyre flow in the area of the northern tip of Madagascar. With such wind profile (Figure 9a) the separation is similar to the separation in the experiment for the southern tip with linear wind (Figure 13e). However here the structure is the inverse, i.e. near the boundary there is a layer with positive relative vorticity in the frictional sublayer, and a layer with negative vorticity in the inertial sublayer.

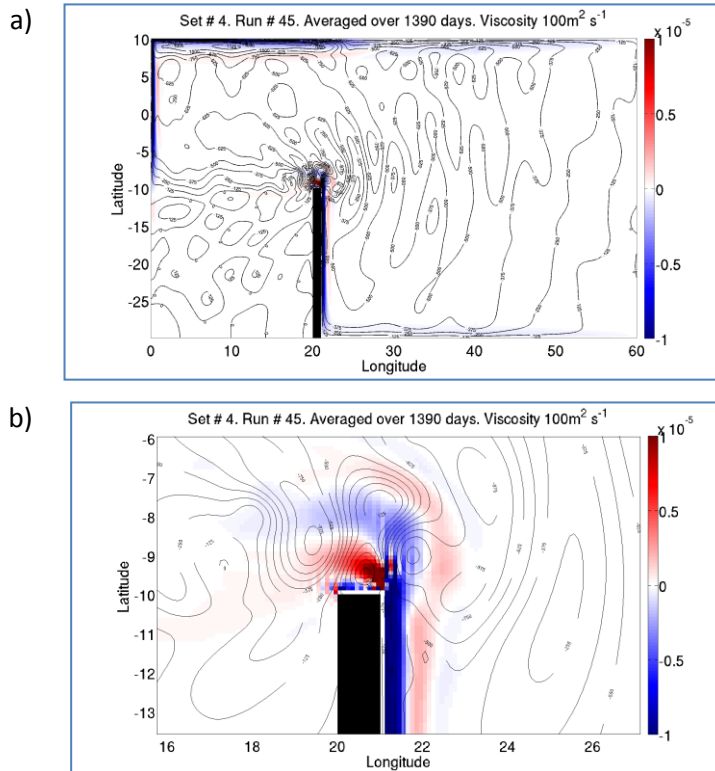


Figure 38. a) Same as for Figure 13. The viscosity is  $100 \text{ m}^2 \text{ s}^{-1}$ . b) Zoom in to the area of separation.

Figure 38 shows a dipole-like structure at the northern tip. After separation, flow propagates westward and then joins the Sverdrup circulation. This flow pattern does not correspond to the realistic case; however this experiment was constructed to see if dipoles might be generated with the simple wind profile in the same manner as for the southern tip.

### 5.4.2. Convergent wind profile

The next wind structure (Figure 9b) is closer to the realistic case (Figure 1) and produces two gyre systems with negative vorticity input in the northern zone and positive in the southern one. With this wind configuration a westward jet is generated in the middle of the basin near the northern tip. In order to explore a behavior of the separation depending on the position of the jet, a series of experiments were made (Figure 39). While moving the zero wind curl position, the magnitude of the curl remains the same, so this variation works as parallel shifting.

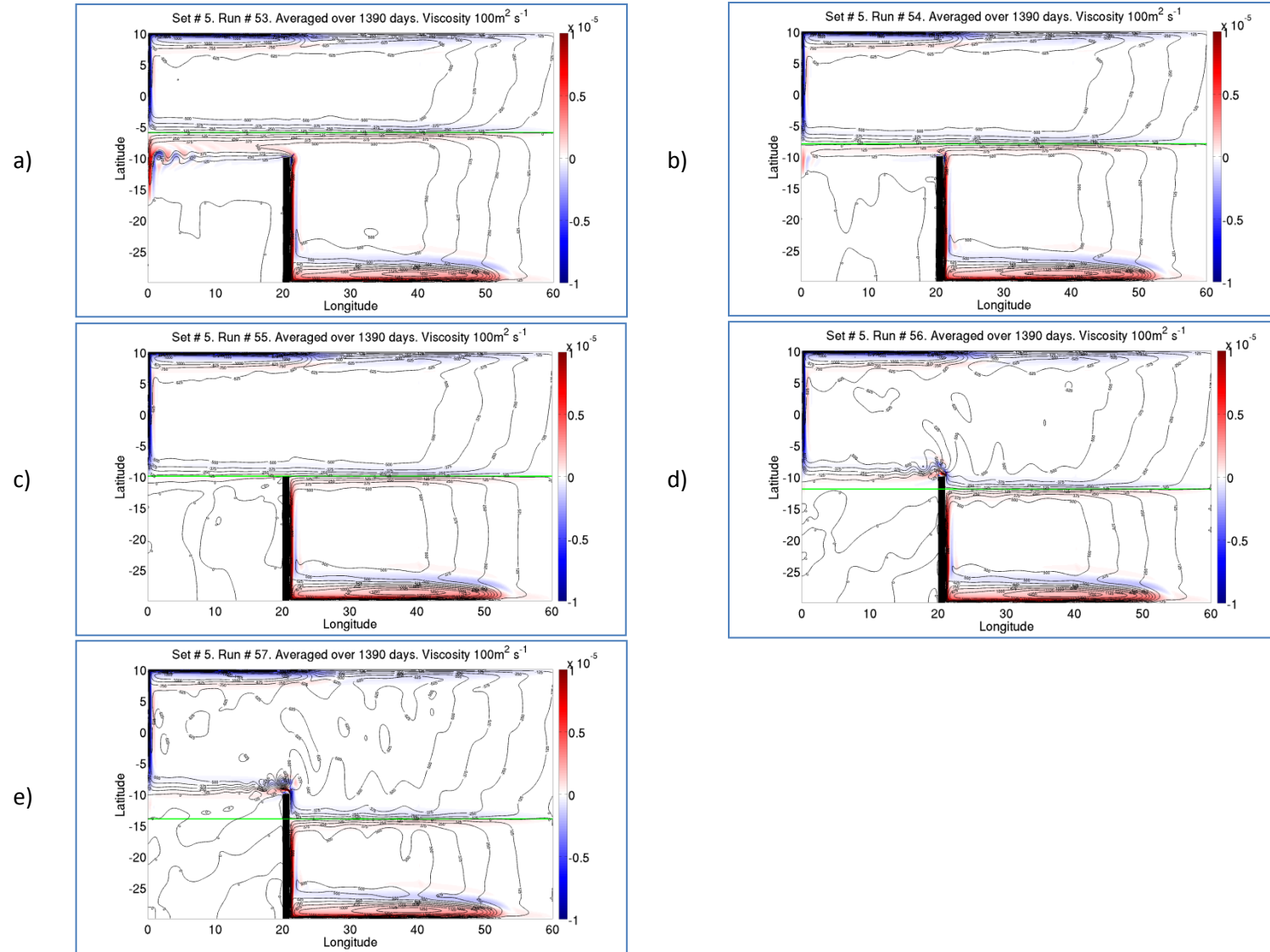


Figure 39. Experimental set # 5. Description is same as in Figure 13 but the viscosity  $100\text{m}^2\text{s}^{-1}$ . Zero wind curl position marked by green line. No-slip.

It is clear from these experiments that when the zero wind curl line is located quite far to the north from the tip (Figure 39a), the circulation in the southern gyres is anticyclonic and after the flow reaches 10°S at the domain western boundary, it turns to the east. Having approached the land, flow follows its boundary and then joins the interior.

When the 'wind' line coincides with the end of the northern tip, two separate gyre are observed and there are no eddies. However, once this line is shifted more to the south, the northward western boundary current appears and starts shedding eddies (Figure 39d). The more to the south the zero wind curl line is shifted, the more intensive dynamics are observed at the tip. To verify the last statement quantitatively, the eddy kinetic energy (EKE) is calculated for two experiments (Figure 39d), Figure 39e).

This quantity is defined as

$$EKE = \frac{u'^2 + v'^2}{2} \quad (1.15)$$

where  $u'$  and  $v'$  are the zonal and meridional velocity anomalies respectively. Once EKE is calculated for each time step it is averaged over 1390 days.

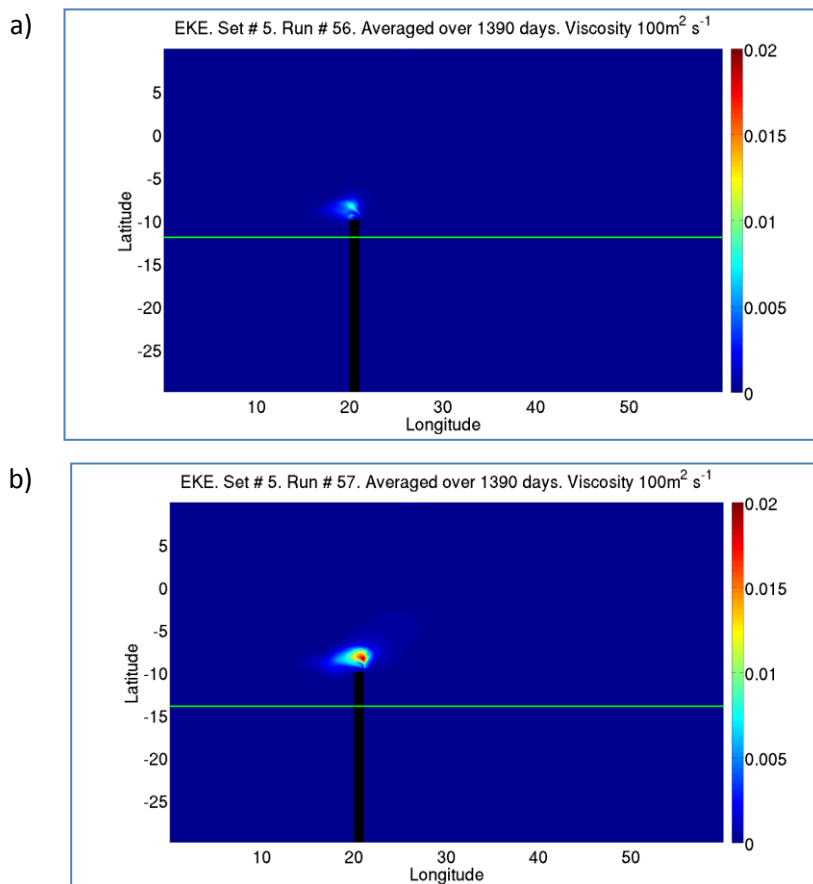


Figure 40. EKE pattern for experimental set # 5. Colors are in  $m^2 s^{-2}$ .

Figure 40 indicates that, in the case where the zero wind curl line is at 14°S the system is more energetic in comparison with the case where the wind line is at 12°S. When flow travels a longer distance along the no-slip boundary, it gains a more anomalously high PV due to the generation of relative vorticity in the frictional sublayer. Also an anomalously low PV is within the inertial sublayer. The more to the south a boundary current starts, the stronger anomaly exists in the inertial sublayer because it drags water of southern origin to the north. In order to get out of such an anomaly before joining the interior, the flow needs to decrease PV, thus it starts shedding eddies.

## 6. Summary and main conclusions

The leading questions that were addressed in the beginning of this thesis are 1) to what degree the far field produces different separation characteristics: dipole formation, a free jet or retroflection; and 2) what kind of lateral boundary conditions either no-slip or free slip is more suitable for simulating reality in numerical modeling.

In section 2 it is shown that the shedding eddies from the SEMC are in the form of dipoles (Figure 6). Although they are not fully symmetric the normalized integral of relative vorticity across the dipole's pathway is around zero. That gives a reason to consider the WBC as a source for these dipoles, if the Stewart constraint (1989) is valid for the WBL, because in this case the flow would retain its integral characteristics after separation. The resolution of altimetry data does not allow checking the suitability of the Stewart constraint (1989) for the WBL, but it does for the dipoles after the separation.

Section 5 describes in detail numerical experiments with several wind profiles which are taken for the far field forcing; also it shows the different behavior of separation under slip and no-slip boundary conditions. To answer the first leading question, it is demonstrated that all three types of separation may be modeled with the linear or piecewise linear far field wind forcing when applied only on the eastern part of the domain. Namely: shedding eddies for the case of the SEMC (with the far field forcing as on Figure 8a), retroflection with a leakage in the form of dipoles for the Agulhas current system (with the far field forcing as on Figure 8b), Figure 8c) and the steady jet for the NEMC (with the far field forcing as on Figure 9a), Figure 9b).

Applying no-slip BC it is shown that, depending on the wind profile, different flow structures are organized. The generation of dipoles takes place (Figure 13) when linear wind is applied. Their direction of propagation is always to the west as a background flow dictates, however the direction of the dipole center line just after separation depends on the viscosity and alters from southwest ( $300\text{m}^2\text{s}^{-1}$ ) to southeast ( $100\text{m}^2\text{s}^{-1}$ ). It is because when viscosity is less the inertia becomes stronger

and the formation of anticyclones occurs at the separation before cyclones are formed. Once the anticyclone has been formed it starts propagating westward and pushing the newly originated cyclone to the north. This makes the orientation of the dipole centre line – southeast. The southwest direction of the centre line for large viscosities is explained in a similar way, but here the frictional boundary sublayer generates cyclones faster than inertial sublayer produces anticyclones.

Under no-slip BC, the flow has irregular behavior at the separation, the westward jet after separation is less visible than in slip cases and is dependent on the viscosity. With the viscosity less than  $100 \text{ m}^2\text{s}^{-1}$ , the small scale variations which are introduced to the system totally break down the westward jet (visible from snapshots, not shown in the report). The period of dipole generation is correlated to the period of the basin modes; however the signal is not regular. The separation position is always at the southern tip if viscosity changes. Nevertheless, if the viscosity value is small ( $100 \text{ m}^2\text{s}^{-1}$ ), some perturbations start propagating upstream. Their period agrees with the period of eddy appearances and basin modes (40-45 days). This disturbance might be considered as additional Rossby waves, which are excited by propagating along the domain boundary perturbations. Moreover, it is shown in sections 5.3.1.2 - 5.3.1.3 that basin modes originate from the barotropic instability of the shear flow located in the domain boundary current in the northeast.

The normalized integral of relative vorticity across the WBL is close to zero ( $10^{-7} \text{ s}^{-1}$ ) in comparison with the fluctuations of relative vorticity field within the WBL ( $10^{-5} \text{ s}^{-1}$ ) and at separation region ( $10^{-6} \text{ s}^{-1}$ ). This value in absolute magnitude is almost the same as the normalized integral of relative vorticity across the westward jet (Figure 29). Also, the normalized integral along the center line of the dipole (Figure 30) is  $3 \cdot 10^{-7} \text{ s}^{-1}$  might also be considered as almost zero. Therefore for the numerical experiments we showed that the Stewart constraint (1989) holds for the WBL and the integrated relative vorticity remains almost the same while flow propagates westward. This analysis supports that dipoles arise from the WBL when no-slip BC is applied.

For the experimental set #2 and #3, we saw that retroflection depends on the zero wind curl line and might be simulated with at least two wind configurations (Figure 8b), Figure 8c). The first one (set #2) induces a clear retroflection for the whole viscosity range when the zero wind curl line is at  $45^\circ\text{S}$ . This structure allows the generation of eddies at the southern tip, some of which are subsequently captured by the return current and dragged to the east. Variation of the zero wind curl line shows different positions of retroflection. Also, with the zero wind curl line at  $43^\circ\text{S}$ , it is possible to generate the northwest orientated dipole along with retroflection. This case is alike the real situation in the Agulhas system.

The third set of experiments produces two-gyre circulations with a return current at the position where the wind curl becomes zero. Regulated by this position, a different geometry of retroflection comes out. When the zero wind line is located at 44°S the flow retroflects at 18°E (which is similar to the second wind type, when the zero curl line is at 41°S) whereas for 42°S, the turning position is 20°E.

As for the slip experiments, the detachment originates when alongshore velocity becomes zero. With decreasing values of viscosity the separation point shifts along the continent first to the west and then to the north. For a small value of viscosity the current wraps around the continent to reach this condition. The less viscosity, the less momentum diffusion which decreases along shore velocity; therefore the flow needs to follow the land boundary longer than it is needed for high values of viscosity. This result corresponds to the slip experiments by Dengg (1992). After the separation the meandering jet propagates to the west until it reaches the domain western boundary and then it goes along the southern boundary and joins the interior. Some recirculation cells are formed at the edges of the jet; they are organized in a staggered order. In contrast with no-slip the main westward jet after separation is always visible independently from viscosity. The formation of meanders has a periodic behavior. The meander generation period is highly connected with the period of the basin modes and is around 40 days which is similar to no-slip. The integral of relative vorticity across the WBL is positive and differs from the integral of relative vorticity across the westward jet that is around zero (Figure 28).

For simulation of the northern tip of Madagascar two wind constructions were used: linear (Figure 9a) and convergent (Figure 9b).

With the linear wind there is a production of the dipoles with the reverse structure that was at the southern tip under linear wind profile with no-slip BC. That is, anticyclones are formed on the 'lee' side of the continents due to frictional sublayer and cyclones come from the inertial sublayer. They propagate to the west with the distinct jet.

With the convergent wind, a two-gyre system is modeled. In this case, the westward jet which passes near the northern tip damps the eddy generation at the northern tip. The closer to the tip a zero wind curl line exists, the more damping emerges (Figure 40).

Thus, to answer the second main question regarding boundary conditions, we showed that slip boundary condition only generates the westward meandering jet with some recirculation cells at the edges after separation, whereas the application of no-slip lateral boundary condition produces counter rotating eddies – dipoles – around the separation point. Therefore under no-slip BC the

model output looks more alike the reality than under free slip BC, even with such simplified wind forcing and geometry of the land.

## **7. Acknowledgments**

I would like to thank Prof. dr. Will de Ruijter and Dewi Le Bars for the inestimable contribution to this work. Enthusiasm and fully involvement of Will and Dewi was a big part of the driving force of this research. I was very lucky to have a team of these two great supervisors.

Furthermore I would like to thank all the students with whom I shared the student room of the IMAU and with whom I swapped ideas about my thesis.

# Appendix

---

## A1. Stream function evaluation

Although there are various schemes of how to compute a streamfunction based on the velocity distribution, the method described in Nencioli et al. (2009) is used here, because streamlines calculated with this method fit more accurately into the relative vorticity patterns than streamlines which are calculated with other algorithms, for instance with the usage of the inbuilt matlab procedure. The main idea of this method is that the streamfunction is calculated as an average of two integrals evaluated on different paths as shown in Figure 41, assuming  $\psi(1,1) = 0$ . For more details on the scheme, please refer to the Appendix of Nencioli et al. (2009). The dimension of streamlines in this case is in  $\text{m}^2/\text{s}$ .

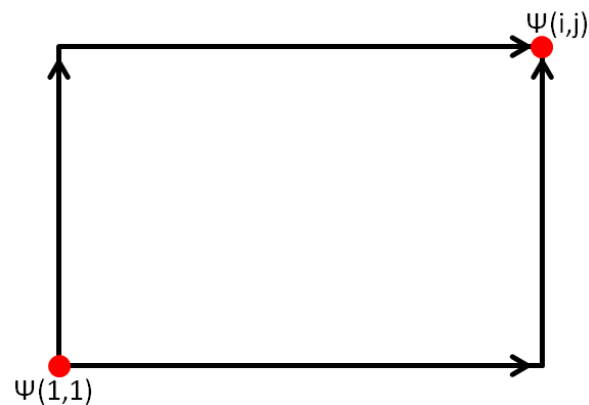


Figure 41. Streamfunction integration paths

## A2. Barotropic instability of the shear flow

In this section the piecewise linear flow (Figure 42) is analysed on the subject of barotropic instability.

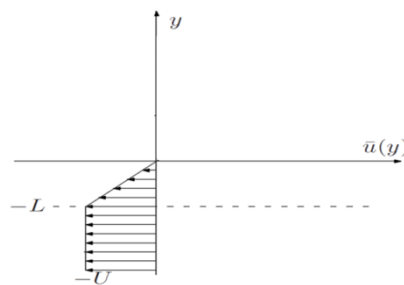


Figure 42. An idealized shear-flow profile that lends to analytic treatment and is likely to produce barotropic instability.

This flow has the following velocity structure

$$\bar{u} = \begin{cases} -U, & y < -L \\ \frac{U}{L}y, & -L \leq y \leq 0 \\ 0, & y > 0 \end{cases} \quad \bar{u}' = \begin{cases} 0, & y < -L \\ \frac{U}{L}, & -L \leq y \leq 0 \\ 0, & y > 0 \end{cases} \quad \bar{u}'' = \begin{cases} 0, & y < -L \\ 0, & -L \leq y \leq 0 \\ 0, & y > 0 \end{cases}$$

where  $U$  is velocity out of the shear and  $L$  is the width of the shear flow.

For barotropic instability, one necessary condition is that the total vorticity of the flow must reach an extremum within the domain, in other words the horizontal gradient of the total vorticity must change sign somewhere within the region (Pedlosky, 1987)

The analysis of the first and second derivative of this velocity distribution shows that although the second derivative vanishes within each of the three segments of the domain; it is nonzero at their junctions (Figure 43). Thus,  $d^2\bar{u}/dy^2$  changes sign in the domain, and this satisfies the condition for the existence of instability. Although instabilities are not guaranteed to exist, we ought to expect them.

Here, theoretical analysis is applied as in Cushman-Rosin and Beckers (2011). If there is instability, in order to find conditions of the wave which has the fastest growing rate, we need to solve the

governing equation in each of the three domain segments  $\frac{d^2\phi}{dy^2} - k^2\phi = 0$ .

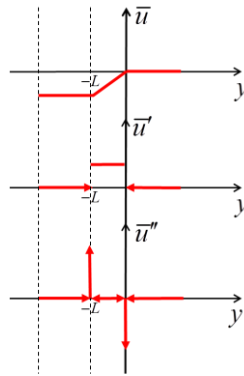


Figure 43. Graphical representation of velocity profile with its second and third derivatives

This equation admits solution

$$\phi = \begin{cases} C_1 e^{ky} + C_2 e^{-ky}, & y < -L \\ C_3 e^{ky} + C_4 e^{-ky}, & -L \leq y \leq 0 \\ C_5 e^{ky} + C_6 e^{-ky}, & y > 0 \end{cases}$$

Now we need to apply six conditions to find six integration constants.

First,  $\phi$  is required to vanish at large distances. Therefore

$$\phi(-\infty) = \phi(+\infty) = 0$$

$$C_2 = C_5 = 0$$

Then,  $\phi$  has to be continuous at each junction

$$\phi(-L - \varepsilon) = \phi(-L + \varepsilon)$$

$$\phi(0 - \varepsilon) = \phi(0 + \varepsilon)$$

And the final one, the integration of a governing equation across the lines joining the domain segments must be continuous at both  $y = -L$  and  $y = 0$

$$\int_{-L-\varepsilon}^{-L+\varepsilon} \left[ (\bar{u} - c) \frac{d^2\phi}{dy^2} - k^2(\bar{u} - c)\phi - \frac{d^2\bar{u}}{dy^2} \phi \right] dy = 0$$

$$\int_{-\varepsilon}^{\varepsilon} \left[ (\bar{u} - c) \frac{d^2\phi}{dy^2} - k^2(\bar{u} - c)\phi - \frac{d^2\bar{u}}{dy^2} \phi \right] dy = 0$$

Nonzero perturbation exists when a system of these six equations admits a nontrivial solution – that is, when the determinant vanishes. Omitting some algebra, the solution for  $c$  is

$$c = -\frac{U}{2} \pm \frac{Ue^{-2kL} \sqrt{e^{2kL} k^2 L^2 (-1 + e^{2kL} (kL - 1)^2)}}{2k^2 L^2}$$

Based on this formula we have two possibilities for  $c$ : totally real and a combination of a real and imaginary part. In the first option we will deal with travelling waves without growth. The second variant gives travelling waves with exponential growth.

Consider the second variant, where  $c$  consists of real and imaginary parts. Then for the term  $\sqrt{e^{2kL} k^2 L^2 (-1 + e^{2kL} (kL - 1)^2)}$  to be imaginary the term  $[-1 + e^{2kL} (kL - 1)^2]$  should be negative, in other words we will have an imaginary solution for  $c$  if

$$(kL - 1)^2 < e^{-2kL}$$

The geometrical solution of the equation  $(kL - 1)^2 - e^{-2kL} = 0$  is shown below

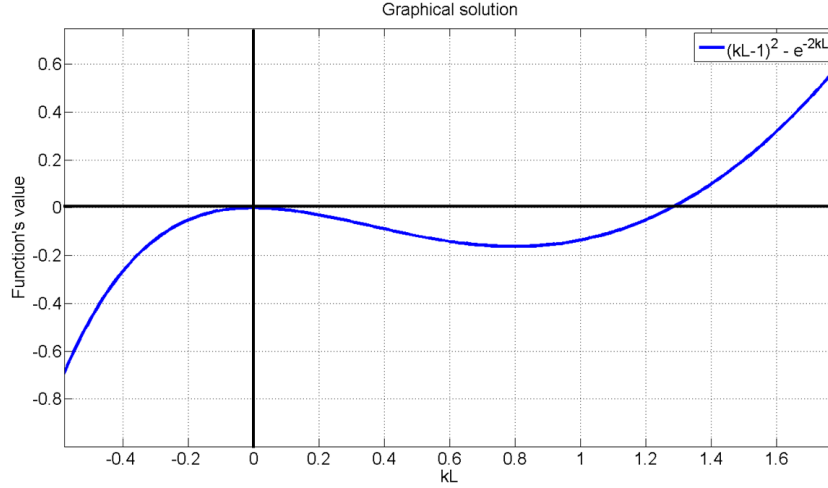


Figure 44 Graphical solution of equation  $(kL-1)^2 - e^{-2kL} < 0$

So, we have an imaginary  $c$  only if  $kL < 1.2785$ , therefore the critical wavenumber is  $k = 1.2785/L$  which separates stable from unstable waves.

Further, it is worth looking for the value of  $k$  which maximizes  $kc_{im}$ . Therefore, we need to analyze the function

$$f = \frac{ke^{-2kL} \sqrt{e^{2kL} k^2 L^2 (-1 + e^{2kL} (kL-1)^2)}}{2k^2 L^2} \quad (*)$$

Substitution of  $kL = x$  simplifies the function. Therefore the behavior of the function (\*) is the same as

$$\tilde{f} = \frac{xe^{-2x} \sqrt{e^{2x} x^2 (-1 + e^{2x} (x-1)^2)}}{2x^2} \text{ up to a multiplication constant } (1/L).$$

The graphic of this function  $\tilde{f}$  is on Figure 45. This function has a maximum imaginary part when  $kL = 0.7970 \approx 0.8$ , this means that the wavelength of the fastest growing mode is

$$\lambda_{fastest\_growth} \approx 7.88L$$

Based on this we found that for such piecewise linear shear flow, the wavelength of the fastest growing perturbation that dominates the early stage of instability is about eight times the width of the shear zone.

$$x \exp(-2x) \times \frac{\sqrt{\exp(2x) x^2 (-1 + \exp(2x) (x-1)^2)}}{2x^2}$$

Exact result:

$$\frac{e^{-2x} \sqrt{e^{2x} (e^{2x} (x-1)^2 - 1) x^2}}{2x}$$

Plots:

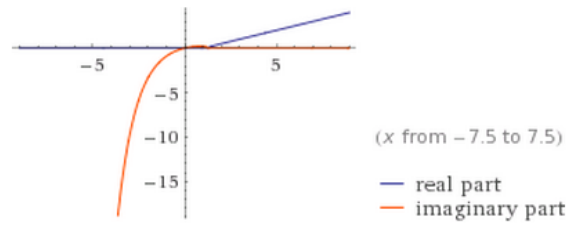
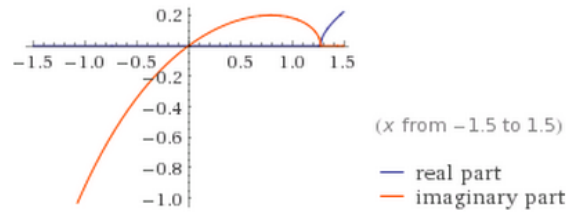


Figure 45. Graphical solution of equation (\*) to find value of  $k$  that maximizes  $kc_{im}$ .

## References

1. Backeberg, B. C., Penven, P., Rouault, M. 2012. Impact of intensified Indian Ocean winds on mesoscale variability in the Agulhas system. *Nature Climate Change*, Letters, 8 July 2011, 1-5.
2. Chassignet E. P., Marshall D.P. Gulf Stream Separation in Numerical Ocean Models. 2008. *Ocean Modeling in an Eddy Regime*, Geophysical Monograph Series 177, 39 – 61.
3. Cushman-Roisin, B., Beckers, J.-M. 2011. Introduction to Geophysical Fluid Dynamics: Physical and Numerical Aspects. *ELSEVIER*.
4. De Ruijter, W. P. M., Biastoch, A., Drijfhout, S. S., Lutjeharms, J. R. E., Matano, R. P., Pichevin, T., van Leeuwen, P. J., Weijer, W. 1999. IndianAtlantic interocean exchange: Dynamics, estimation and impact, *J. Geophys. Res.*, 104, 20885 – 20910.
5. De Ruijter, W. P. M., van Aken, H. M., Beier, E. J., Lutjeharms, J. R. E., Matano, R. P., Schouten, M. W. 2004. Eddies and dipoles around South Madagascar: Formation, pathways and large scale impact. *Deep-Sea Res. I*, 51, 383–400.
6. Dengg, J. The problem of Gulf Stream Separation: A Barotropic Approach. 1992. *Journal of physical oceanography*. Volume 23, 2128 – 2200.
7. Dijkstra, H.A. 2008. Dynamical Oceanography. *Springer*.
8. Fu, L.-L., Chelton, D.B., Le Traon, P.-Y., Morrow, R. 2010. Eddy dynamics from satellite altimetry. *Oceanography* 23(4), 14–25.
9. Gründlingh, M. L. 1995. Tracking eddies in the southeast Atlantic and southwest Indian oceans with TOPEX/POSEIDON. *Journal of Geophysical Research: Oceans (1978–2012)*, Volume 100, Issue C12, 24977–24986.
10. Hallberg, R. 1997. HIM: The Hallberg Isopycnal Coordinate Primitive Equation Model.
11. Hallberg, R. 2005. A thermobaric instability of Lagrangian vertical coordinate ocean models. *Ocean Modelling*, 8, 279-300.
12. Kiss, A.E. Potential vorticity “crises”, adverse pressure gradients, and western boundary current separation. 2002. *Journal of Marine Research*, 60, 779-803.
13. LaCasce, J. H., Isachsen, P. E. 2007. On Sverdrup Discontinuities and Vortices in the Southwest Indian Ocean. *Journal of Physical Oceanography*, Volume 37, 2940-2950.
14. Lutjeharms, J. R. E. 1976: The Agulhas Current System During the Northeast Monsoon Season. *J. Phys. Oceanogr.*, 6, 665–670.
15. Lutjeharms, J.R.E. 1981. Features of the southern Agulhas Current circulation from satellite remote sensing. *S. Afr. J. Sci.* 77, 231-236.
16. Munk W. H. 1950. On the wind driven ocean circulation.. *Journal of Meteorology*. Vol. 7, No. 2. 79 – 93.

17. Nakano, H., Tsujino H., Furue R. The Kuroshio Current System as a jet and twin "relative" recirculation gyres embedded in the Sverdrup circulation. *Dynamics of Atmospheres and Oceans*, 45,135–164.
18. Nencioli, F., Dong, C., Dickey, T.D., Washburn, L., McWilliams, J.C. 2010. A Vector Geometry Based Eddy Detection Algorithm and Its Application to a High-resolution Numerical Model Product and High-frequency Radar Surface Velocities in the Southern California Bight. *Journal of Atmospheric and Oceanic Technology*, Vol 27, No 3, 564-579.
19. Pedlosky, J. 1987. Geophysical fluid dynamics. *Springer*.
20. Pedlosky, J. 1996. Ocean circulation theory. *Springer*.
21. Quartly, G. D., Buck, J. J. H., Srokosz, M. A., and Coward, A. C. 2006. Eddies around Madagascar – the retroflexion reconsidered. *J. Mar. Syst.*, 63, 115–129.
22. Ridderinkhof, W., Le Bars, D., von der Heydt, A. S., and de Ruijter, W. P. M. Dipoles of the South East Madagascar Current. *Geophysical Research Letters*, VOL. 40, 558–562.
23. Stewart, R.W. No-slip Constraint and ocean models. 1989. *Atmosphere-Ocean*, 27:3, 542-552.